Somatic genetic rescue of a germline ribosome assembly defect

Shengjiang Tan, Laëtitia Kermasson, Christine Hilcenko, Vasileios Kargas, David Traynor, Ahmed Boukerrou, Norberto Escudero-Urquijo, Alexandre Faille, Alexis Bertrand, Maxim Rossmann, et al.

Somatic genetic rescue of a germline ribosome assembly defect

Shengjiang Tan,[1,2,3,*], Laëtitia Kermasson[4,*], Christine Hilcenko[1,2,3], Vasileios Kargas[1,2,3], David Traynor[1,2,3], Ahmed Z Boukerrou[1,2,3], Norberto Escudero-Urquijo[1,2,3], Alexandre Faille[1,2,3], Maxim Rossmann[1,2,3], Beatriz Goyenechea[3,§], Alexis Bertrand[4], Jonathan Moreil[4], Olivier Alibeu[5], Blandine Beaupain[6], Christine Bôle-Feysot[5], Stefano Fumagalli[7,8], Sophie Kaltenbach[9,10], Jean-Alain Martignoles[11], Cécile Masson[12], Patrick Nitschké[12], Mélanie Parisot[5], Aurore Pouliet[5], Isabelle Radford-Weiss[9,10], Frédéric Tores[12], Jean-Pierre de Villartay[4], Mohammed Zarhrate[5], Peter J Bond[13,14], Christine Bellanné-Chantelot[15], Isabelle Callebaut[16,°], François Delhommeau[11,°], Jean Donadieu[17,°], Alan J Warren[1,2,3,@,#], Patrick Revy[4,@,#]

[1]Cambridge Institute for Medical Research, Cambridge Biomedical Campus Keith Peters Building, Hills Rd, Cambridge CB2 0XY, United Kingdom.
[2]Wellcome Trust-Medical Research Council Stem Cell Institute, Jeffrey Cheah Biomedical Centre, Puddicombe Way, Cambridge Biomedical Campus, Cambridge, CB2 0AW, UK.
[3]Department of Haematology, University of Cambridge School of Clinical Medicine, Jeffrey Cheah Biomedical Centre, Puddicombe Way, Cambridge Biomedical Campus, Cambridge, CB2 0AW, UK.
[4]Université de Paris, Imagine Institute, Laboratory of Genome Dynamics in the Immune System, Equipe Labellisée Ligue contre le Cancer, INSERM UMR 1163, F-75015, Paris, France.
[5]INSERM Unité Mixte de Recherche 1163, Structure Fédérative de Recherche Necker INSERM US24/CNRS UMS3633, Genomic Core Facility, Paris Descartes-Sorbonne Paris Cité University, Imagine Institute, Paris, France.
[6]French Neutropenia Registry, Assistance Publique-Hôpitaux de Paris, Trousseau Hospital, Paris, France.
[7] Institut Necker Enfants Malades, Paris, France.
[8] INSERM, U1151, Université Paris Descartes Sorbonne Cité, Paris, France.
[9] Université Paris Descartes, Faculté de Médecine Sorbonne Paris Cité.
[10]Service de cytogénétique, Hôpital Necker, Assistance Publique-Hôpitaux de Paris.
[11]Sorbonne Université, Inserm, Centre de Recherche Saint-Antoine , AP-HP, Hôpital Saint-Antoine, Hématologie Biologique, F-75012 Paris.
[12]INSERM Unité Mixte de Recherche 1163, Bioinformatics Platform, Paris Descartes-Sorbonne Paris Cité University, Imagine Institute, Paris, France.
[13]Bioinformatics Institute (A*STAR), 30 Biopolis Street, 07-01 Matrix, Singapore 138671, Singapore
[14]Department of Biological Sciences, National University of Singapore, 14 Science Drive 4, Singapore 117543, Singapore.
[15]Dept of Genetics, Pitié-Salpêtrière Hospital, Sorbonne University, Paris, France.
[16]Sorbonne Université, Muséum National d'Histoire Naturelle, UMR CNRS 7590, Institut de Minéralogie, de Physique des Matériaux et de Cosmochimie, IMPMC, 75005 Paris, France.
[17]Service d'Hémato-Oncologie Pédiatrique, Assistance Publique-Hôpitaux de Paris Hôpital Trousseau, Registre des neutropénies-Centre de référence des neutropénies chroniques, Paris, France.
[§]Current address: PolyProx Therapeutics, Babraham Research Campus, Cambridge, CB22 3AT, UK.

* Joint first authors
° These authors contributed equally to the study
Corresponding author
@ Co-senior authors

List of supplementary data

Abstract

Indirect somatic genetic rescue (SGR) of a germline mutation is thought to be rare in inherited Mendelian disorders. Here, we establish that acquired mutations in the *EIF6* gene are a frequent mechanism of SGR in Shwachman-Diamond syndrome (SDS), a leukemia predisposition disorder caused by a germline defect in ribosome assembly. Biallelic mutations in the *SBDS* or *EFL1* genes in SDS impair release of the anti-association factor eIF6 from the 60S ribosomal subunit, a key step in the translational activation of ribosomes. We identified diverse mosaic somatic genetic events (point mutations, interstitial deletion, reciprocal chromosomal translocation) in SDS hematopoietic cells that reduce eIF6 expression or disrupt its interaction with the 60S subunit, thereby conferring a selective advantage over non-modified cells. SDS-related somatic *EIF6* missense mutations that reduce eIF6 binding to the 60S subunit suppress the defects in ribosome assembly and protein synthesis in multiple SBDS-deficient species including yeast, *Dictyostelium* and *Drosophila*. Our data suggest that SGR is a universal phenomenon that may influence the clinical evolution of diverse Mendelian disorders and support eIF6 suppressor mimics as a therapeutic strategy in SDS.

Introduction

In normal individuals, somatic mutations and chromosomal alterations accumulate with age in cells from diverse tissues, including the hematopoietic system[1-9]. The accumulation of spontaneous genetic variations may contribute to age-related disease, organismal aging, and tumorigenesis[10,11]. However, more than 40 years ago, Weill and Reynaud proposed that in certain circumstances, somatic mutations might be beneficial to the cell without inducing disease or cellular transformation[12]. In inherited Mendelian diseases, this phenomenon, dubbed somatic genetic rescue (SGR)[1], is considered rare and has mainly been observed in hematopoietic disorders, where it may confer a selective advantage and promote recovery of hematopoiesis by counteracting the deleterious effect of the germline mutation[14-16]. In most cases, SGR affects the germline mutated gene (direct SGR[13]). In contrast, indirect SGR involves the acquisition of somatic mutations in a distinct gene that participates in the same pathway that is altered by the germline mutation[13]. For instance, indirect SGR has been highlighted in three independent studies on telomeropathies where somatic promoter-activating mutations in *TERT,* the gene encoding the telomerase catalytic subunit that elongates telomeres, were identified in blood cells from patients with germline mutations in genes involved in telomere length regulation, *i.e. TERC*, *PARN* and *NHP2*[17-19]. To the best of our knowledge, indirect SGR has only been described to date in the telomeropathies.

Shwachman-Diamond syndrome (SDS; OMIM #260400) is a rare autosomal recessive disease characterized by bone marrow failure, poor growth, skeletal defects, exocrine pancreatic insufficiency, and predisposition to hematological malignancies[20]. Biallelic mutations in *SBDS* are the predominant cause of SDS, but biallelic *EFL1* mutations have also been identified [2]. SBDS and the GTPase EFL1 cooperate to evict the anti-association factor eIF6 (yeast Tif6) from the nascent large ribosomal subunit[23-25], an essential prerequisite that allows the 60S and 40S subunits to join to form mature actively translating 80S ribosomes. Hence SBDS and EFL1 deficiencies are considered as ribosomopathies since they lead to impaired ribosomal subunit joining and reduced protein synthesis as a consequence of defective eIF6 eviction from the 60S subunit[20, 23].

Recurrent mosaic acquired interstitial deletions of chromosome 20 (del(20q)) encompassing the *EIF6* gene have been detected in bone marrow cells from some individuals with SDS[3]. This observation led to the proposal that a reduced dose of eIF6 due to del(20q) might be advantageous to SDS cells by bypassing the defect in ribosomal subunit joining, representing a novel mechanism of indirect SGR[13, 26-28]. However, the minimal del(20q) region characterized in SDS hematopoietic cells in SDS spanned 2.2 Mb, encompassing 28 genes in addition to *EIF6*[28]. Furthermore, del(20q) is one of the most common mosaic chromosomal alterations (mCAs) associated with age-related clonal hematopoiesis[7-9]. Thus, it remains unclear whether *EIF6* haploinsufficiency generated by del(20q) indeed represents a *bona fide* mechanism of indirect SGR in SDS hematopoietic cells.

Here, we hypothesize that acquired somatic mutations in the *EIF6* gene might provide a selective advantage for hematopoietic stem and progenitor cells (HSPCs) in SDS that promotes their clonal expansion. To test this hypothesis we performed ultra-deep sequencing of the *EIF6* gene in hematopoietic cells from 40 individuals with SDS carrying biallelic germline *SBDS* mutations. We identified mosaic somatic *EIF6* mutations in 60 % of SDS patients but not in healthy donors. By combining structural modelling and molecular dynamics (MD) simulations with functional studies in yeast, *Dictyostelium discoideum* and *Drosophila melanogaster*, we establish that conserved *EIF6* missense mutations that map to the interface with the 60S subunit bypass SBDS deficiency by reducing the affinity of eIF6 and rescuing the defects in ribosome assembly and global protein synthesis. Our results establish that acquisition of somatic *EIF6* mutations is a frequent mechanism of indirect somatic genetic rescue in hematopoietic cells in SDS, suggesting a strategy for the development of disease-modifying targeted therapeutics in SDS.

Results

EIF6 mutations as a mechanism of somatic genetic rescue in SDS.

To determine whether acquired mutations in *EIF6* represent a mechanism of SGR in hematopoietic cells in SDS, we performed ultra-deep targeted sequencing of the full genomic *EIF6* gene (introns/exons) after hybridization-based capture with biotinylated ssDNA probes designed and prepared to target a 123 kb chromosomal locus encompassing *EIF6* (chr20:35,256,992-35,380,631 according to the GRCh38.p12 assembly of the human reference genome). We analyzed a total of 14 SDS patients (hereafter denoted SBDS) carrying biallelic germline mutations in the *SBDS* gene (mean age, 14.7 years; range 1-38.2; DNA extracted from blood n = 8; DNA extracted from bone marrow n = 6; **Suppl. Table S1**). We also tested 5 SDS patients who had undergone hematopoietic stem cell transplantation (denoted SBDS post-HSCT; DNA extracted from blood) and fully reconstituted their hematopoietic system as inferred by wild type (WT) *SBDS* sequence in peripheral blood cells (100 % donor, not shown). In addition, we tested 5 patients with neutropenia of uncharacterized genetic origin (denoted Neutro Unkn; in 4, DNA was extracted from blood, in 1 from bone marrow), one SDS-like patient carrying biallelic *SRP54* mutations[30] (denoted SRP54; DNA from blood), and 15 healthy age-matched donors (denoted Ctl, DNA from blood). After removing duplicates, ultra-deep *EIF6* sequencing provided a mean depth of 2,807X (ranging from 718X to 7,940X). To accurately identify *EIF6* genetic variants with low rates of somatic mosaicism, we considered all detected genetic variants in the *EIF6* coding sequence with variant allele frequencies (VAF) $\geq$ 0.5 % as somatic *EIF6* mutations. Using this criterion, we did not detect *EIF6* mutations in the 15 healthy controls, the 5 SDS patients post-HSCT, the 5 patients with neutropenia from unknown molecular origin or the SRP54-deficient patient. In contrast, we detected a total of 10 *EIF6* mutations in 7 out of the 14 SDS patients (50 %) (**Figure 1A**). Nine mutations corresponded to single nucleotide variation (SNVs; 8 missense and 1 nonsense), while one was a 5 bp deletion predicted to cause a frameshift and a premature stop codon (**Figure 1B**). The combined annotation-dependent depletion (CADD) score represents a predictive indicator of the deleterious effect of a genetic variant[31]. Noticeably, the mean CADD score

for the 9 *EIF6* SNVs identified in SDS patients was significantly higher than the mean CADD score generated by all possible SNVs in the *EIF6* coding sequence (synonymous, missense, nonsense, start/stop loss; **Figure 1C and Suppl. Table S2**). This observation suggests that clones carrying *EIF6* SNVs predicted to have high deleterious impact were preferentially amplified in blood cells from SDS patients. Moreover, the absence of somatic *EIF6* mutations in normal individuals suggests that they are not favored in cells in normal conditions.

The mean VAF of the 10 *EIF6* mutations was 2.15 % (range 0.51-12.32 %). In 3 SDS patients, we detected 2 different *EIF6* mutations (**Figure 1D and Suppl. Table S1**), indicating that distinct *EIF6* mutated clones can emerge independently within the same individual. Strikingly, the same somatic mutation (g.20:33868509A>G; c.317A>G) leading to the eIF6 substitution N106S was detected in four unrelated SDS patients with a VAF ranging from 0.87 to 12.32 %. This suggested to us that N106S might represent a recurrent somatic mutation with a key functional impact in SBDS deficient cells (see below) (**Figure 1D and Suppl. Table S1**).

We next analyzed the B-allele frequency (BAF) across all heterozygous single nucleotide polymorphisms (SNPs) located in the *EIF6* gene. In 9 SDS patients and 10 healthy individuals in whom SNPs were informative, the BAFs were around 0.5 as expected for heterozygous SNPs in diploid cells (**Figure 1E, Suppl. Table S3**)[32]. In contrast, two SDS patients (SBDS-1 and SBDS-9) exhibited a sharp BAF deviation from 0.5 (**Figure 1E, Suppl. Table S3**), suggesting the existence of a mosaic genetic deletion encompassing the *EIF6* gene. The combination of cytogenetic analysis using specific FISH probes located nearby the *EIF6* locus (**Suppl. Fig. 1**) and array comparative genomic hybridization (CGH) confirmed the presence of an interstitial 20q11.21-q13.2 deletion encompassing *EIF6* in a bone marrow sample from patient SBDS-9 that was estimated to affect 37 % of cells (**Figures 1F, G, and Suppl. Table S1**).

Although ultra-deep *EIF6* sequencing did not detect *EIF6* mutations in bone marrow cells from patient SBDS-3, cytogenetic analysis highlighted a reciprocal translocation t(16;20)(q24;q11.2) in 2 out of 20 metaphases (**Suppl. Table S1 and not shown**). Since the *EIF6* gene maps to 20q11.2,

we wondered whether the breakpoint in chromosome 20 was located within the *EIF6* gene. A search for chimeric reads from the ultra-deep sequencing containing both the *EIF6* gene and chromosome 16 sequences unveiled chimeric sequences in SBDS-3 but not in 4 controls. Analysis of chimeric reads precisely positioned the translocation breakpoints in chromosome 20 within intron 4-5 of *EIF6* and in a non-coding region of chromosome 16 between the *COX4* (9,175 bp at 5' side) and the *IRF8* genes (86,642 bp at 3' side) (**Figure 1H**). We conclude from this analysis that the translocation t(16;20)(q24;q11.2) detected in a mosaic state in bone marrow cells from SBDS-3 disrupted one copy of *EIF6* to cause haploinsufficiency.

We conclude that multiple distinct somatic genetic events affecting the *EIF6* gene are frequent in hematopoietic cells in SDS but not in healthy individuals. These *de novo* mosaic genetic modifications consist of chromosomal alterations affecting *EIF6* (interstitial del(20q), reciprocal translocation) or somatic point mutations in the *EIF6* coding sequence (nonsense, missense, and small deletions). These findings support our hypothesis that *EIF6* mutations indeed represent a mechanism of indirect SGR that promotes clonal expansion in the context of a germline ribosome assembly defect in SDS.

Spectrum of acquired somatic *EIF6* mutations in SDS

To strengthen this initial genetic analysis and identify further somatic *EIF6* mutations, we performed ultra-deep *EIF6* sequencing of a larger cohort consisting of 26 SDS patients carrying biallelic *SBDS* mutations (mean age: 15.4 years, range 0.47-52.2 years; DNA from blood cells n = 3; DNA from bone marrow n = 23, **Suppl. Table S1**) and 25 age-matched healthy individuals (DNA from blood cells, n = 25). To increase the depth of sequencing with a limited quantity of DNA, we modified the hybridization-based capture strategy by using the *EIF6* cDNA (1,016 bp) as sequence bait. After duplicate removal, this approach yielded a mean depth of 26,873X (range 11,140-47,185X). In this setting we considered all genetic variants in the *EIF6* coding sequence with a VAF ≥ 0.25 % as

somatic *EIF6* mutations. In total, we identified 56 *EIF6* mutations in 17 of the 26 SDS patients (65.3 %), but none in the 25 healthy donors (**Figure 2A**). Up to 8 different *EIF6* mutations were present in the same individual (mean 2.07; range 0-8) (**Figure 2B**). The mean VAF in patients carrying *EIF6* mutations was 1.43 % (range 0.25-27.9 %) (**Figure 2C**). Congruent with the reported accumulation of somatic mutations in hematopoietic cells over time[5,6], we found a slight but significant positive linear correlation between the *EIF6* mutation count and age (r = 0.4105; p = 0.0335; Pearson correlation) (**Figure 2D**). However, the cumulative VAF per patient among SDS patients carrying *EIF6* mutations did not correlate with age or mutation count (r = 0.04629; p = 0.86 and r = 0.03589; p = 0.8912, respectively, **Suppl. Figure 2**). Among the 56 *EIF6* mutations, 46 were SNVs (82.1 %) that mainly consisted of C>T transitions (51.1 %), a mutational spectrum that likely reflects the spontaneous deamination of cytosine residues observed in hematopoietic cells from normal individuals[5,6,33] (**Figure 2E**). Thirty-one were nucleotide substitutions leading to missense mutations (55.3 %), 20 corresponded to nonsense or small indels inducing frameshift and premature stop codons (35.7 %), 4 were synonymous (7.1 %) and one corresponded to loss of the start codon (1.8 %; M1L) (**Figure 2F**). The mean CADD score of these 56 SNVs was significantly higher than the mean CADD scores of all possible *EIF6* SNVs (**Figure 2G**). Furthermore, the mutation spectrum among the SNVs highlighted 3.4 times more non-synonymous mutations than expected neutrally, as inferred by the ratio of non-synonymous to synonymous variants (dN/dS = 3.4 ; with dN/dS = 1 representing neutrality)[34]. Together, these results further argue that *EIF6* mutations predicted to have a functional impact are positively selected in hematopoietic cells in SDS.

Collectively, we identified a total of 66 somatic eIF6 mutations in 24 out of 40 SDS patients (60 %) from two independent genetic analyses, of which 54 (81.8 %) are missense mutations (**Figures 3A, B**) that are distributed throughout the protein (**Figure 3C**). Five SDS patients (12.5 %) exhibited clones with a VAF higher than 5 %. The clones with a VAF > 5 % harbored either nonsense (Q93*, VAF= 6.34 %; Q145*, VAF=10 %) or missense *EIF6* mutations (G69D, VAF=27.9 %; R96W, VAF=7.59 %; N106S, VAF=12.32 %) and 19 SDS patients (47.5 %) exhibited a cumulative VAF > 1 % (**Figure 3A and Suppl. Table S1**). Strikingly, 7 amino acids (aa) (N66, G69, R96, N106, D112,

L133 and V135) were recurrently targeted by missense mutations (**Figures 3A, B and Suppl. Table S1**): 6 patients carried 7 SNVs affecting residue G69, generating distinct missense substitutions (G69A; G69S; G69V; G69D) (**Figure 3B**); 4 patients carried the same R96W substitution; 4 patients carried mutations affecting residue N106 (N106S; N106D), 2 patients had mutations affecting residue N66 (N66H; N66K); 2 patients harbored mutations affecting residue D112 (D112N; D112A); 2 patients carried mutations affecting residue L133 (L133P; L133I) and 2 patients harbored the same V135M mutation (**Figure 3B**). Noteworthy, among the somatic missense mutations revealed, G14S and N106S (**Figure 3B**) were previously identified as suppressor mutations that bypassed the ribosome assembly defect in yeast cells lacking the SBDS homolog, Sdo1[25]. These findings further support the notion that our ultra-deep sequencing had identified mutations that drive positive clonal selection in the context of human SBDS deficiency *in vivo,* likely by increasing fitness at the cellular level.

There was no statistical correlation between the presence of *EIF6* mutations (or their VAF) and hemoglobin, platelet or white cell count in SDS individuals at the time of DNA sampling for *EIF6* sequencing (**Suppl. Figure 3 and Suppl. Table S1**).

In sum, our genetic analysis demonstrates that clones carrying somatic genetic mutations in the *EIF6* gene are frequent in blood and bone marrow cells from SDS patients, suggesting that they provide a cellular selective advantage in this context. Some of these events, *i.e.* interstitial deletion, reciprocal translocation, nonsense and small indels are predicted to generate *EIF6* null alleles, provoking *EIF6* haploinsufficiency. However, as the majority of *EIF6* mutations detected by ultra-deep sequencing consisted of missense mutations, we set out to assess their impact by structural, biochemical and functional analysis.

Three mutation hotspots in eIF6

We focused on the eIF6 amino acids (N66, G69, R96, N106, D112, L133, and V135) that are recurrently targeted in SDS. These residues are highly conserved across species, with 5 out of the 7 amino acids conserved from *Homo sapiens* to the archaeon *Methanopyrus kandleri* (**Suppl. Figure 4**). We used the 2.4 Å cryo-EM structure of human eIF6 bound to the human 60S subunit (PDBID: XXX) to map the eIF6 mutations (**Figure 4A**). As first described for the two homologs in *Methanocaldococcus jannaschii* and *Saccharomyces cerevisiae*[37], eIF6 has a pentein fold consisting of five repeated subunits, with 3-stranded ß-sheets arranged as blades around a five-fold axis of pseudo-symmetry (**Figure 4A**). The radial arrangement of these subunits is closed by a "velcro" strategy, with the last ß-strand of the last blade provided by the N-terminal ß-strand, as in ß-propeller 3D structures. Five small helices form an inner ring that includes a position invariably occupied by a small amino acid residue (G, A) to allow tight packing (**Figure 4A**, **Suppl. Figure 4**). Both sides of the pentein fold form flat surfaces, one of which forms the interface with ribosomal proteins uL14 (RPL23), eL24 (RPL24), uL3 (RPL3) (using the new nomenclature[4]) and the sarcin-ricin loop (SRL) (**Figure 4A**). We mapped the seven recurrently mutated amino acids to three main hotspots. The first hotspot (highlighted in black in **Figure 4A**), includes residue N106 (blade 3) which is mutated (N106S and N106D) in 6 SDS individuals (**Figure 3B**). The side chain of N106 forms hydrogen (H)-bonds with the main chain oxygen atoms of uL14 residues A133 and A136 (**Figure 4B**). In addition, the backbone nitrogen of N106 forms an intra-molecular H-bond with the backbone oxygen of residue A103. In turn, the backbone nitrogen of A103 forms an H-bond with the backbone oxygen of uL14 residue G137. The side chain and backbone atoms of N106 also form intra-protein H-bonds with the side-chain and backbone atoms of R61 (blade 2) (**Figure 4B)**. A network of H-bonding interactions links R61 (blade 2) with the main chain oxygen atoms of G14 (blade 1), I58 and G60 (blade 2) and G149 (blade 4) (**Figure 4C**). Interestingly, an R61L mutation was recently identified in a patient with an SDS-like clinical phenotype[5]. The second hotspot (highlighted in cyan in **Figure 4A**) contains 5 aa that cluster at the interface between blade 2 (N66 and G69) and blade 3 (D112, L133 and V135) (**Figure 4D**). Residue N66 forms H-bonds with the main chain oxygen atoms of G69 and L133, while

the side chains of L133 and V135 form hydrophobic interactions. At the solvent exposed core of eIF6, D112 forms H-bonds with the backbone nitrogen of R67 and the side chain of N156 (blade 4) as part of a wider network of H-bonds involving residues N21 (blade 1), N111 (blade 3) and D201 (blade 5) (**Figure 4E**). Mutation of any of the five residues lying within the second hotspot is predicted to destabilize the pentein fold as a whole. The third hotspot (highlighted in red in **Figure 4A**) contains residue R96 (at the end of strand ß3 of blade 2), that forms an intra-protein H-bond with the backbone of residue T76 (blade 2) (**Figures 4F**). This interaction may help promote polar interactions between eIF6 residue D78 (blade 2) and eL24 residue K2. The recurrent R96W mutation, identified in 4 SDS patients, likely disrupts both the stability of blade 2 and the interaction of eIF6 with eL24.

EIF6 **mutations rescue fitness defect of SBDS-deficient cells** ***in vivo***

We next set out to test the impact of the N66H, G69S, R96W, N106S, D112N, L133P, and V135M mutations on eIF6 protein expression, stability and function. Immunoblotting of extracts from HEK293T cells transfected with equal amounts of WT and mutant FLAG-tagged eIF6-expressing vectors indicated that all but the N106S mutation reduced eIF6 expression, consistent with a reduction in eIF6 stability as predicted by the structural analysis (**Figure 5A**). We further verified that the ectopic expression of the FLAG-eIF6 N106S mutant did not affect the expression and/or stability of the endogenous eIF6 protein (**Figure 5B**). These observations suggest that the selective advantage provided by the N106S mutation (**Figures 5A, B)** is not due to reduced eIF6 dosage, in contrast to the N66H, G69S, R96W, D112N, L133P, and V135M variants.

We assessed the ability of the eIF6 N106S mutant to interact with the 60S subunit. Immunoblots of sucrose gradient fractions from HEK293T cells transfected with vectors expressing either WT FLAG-eIF6 or N106S proteins indicated that unlike WT FLAG-eIF6, the N106S mutant did not co-sediment with the 60S subunit (**Figures 5C, D**). We next examined the distribution of WT eIF6 versus the mutants T56K (the most potent gain-of-function mutation identified in yeast[6]) and

N106S when expressed in *Dictyostelium discoideum* Ax2 cells lacking the endogenous *EIF6* allele by sucrose gradient fractionation and immunoblotting of cell extracts (**Figure 5E**). Both the endogenous and over-expressed WT eIF6 but not the eIF6-T56K or N106S variants, co-fractionated with the 60S subunit. Furthermore, WT eIF6 but not the T56K or N106S variants, induced a functional defect in ribosomal subunit joining in Ax2 cells.

We directly tested the ability of SDS-associated eIF6 missense mutations to rescue the fitness defect of SBDS-deficient cells *in vivo* by engineering a conditional mutation in the yeast SBDS homolog Sdo1 (*sdo1*^{ts}), based on a temperature-sensitive intein which is spliced out to create a functional Sdo1 protein at the permissive (23 °C) but not the restrictive temperatures (30 °C or 37 °C)[7]. Compared with empty vector or WT Tif6 controls, expression of the Tif6-G14S, R61L and N106S mutants (but not G69S, R96W, D112E, L133P and V135M), rescued the fitness defect of *sdo1*^{ts} cells at the restrictive temperatures (**Figure 5F**). Immunoblotting revealed that all but the G14S, R61L and N106S mutations reduced the expression of Tif6 compared with the endogenous Tif6 protein (**Figure 5G**). These data confirm that SDS-related Tif6 missense mutations that map to the interface with uL14 act as dominant gain-of-function mutations that are able to bypass the fitness defect caused by Sdo1 deficiency and suggest that mutations that destabilise the Tif6 protein confer loss of function. Given the conservation of eIF6 function from human to prokaryotes, these observations collectively support the hypothesis that in SDS, HSPCs positively select somatic mutations that either impair the interaction of eIF6 with the 60S subunit or reduce eIF6 expression.

N106S mutation dynamically disrupts the H-bonding interface between eIF6 and uL14

To provide additional insights into the mechanism by which the SDS-related eIF6 missense mutation N106S destabilizes the interaction interface with uL14, we utilized atomic-resolution MD simulations to study the stability of a solvated complex comprising eIF6, uL14, eL24, uL3 and a double stranded helical segment of the 28S ribosomal RNA. Three 500 ns replica simulations were

performed for both the WT system and the in silico eIF6 N106S mutant (**Figures 6A-F**). In the WT simulations, the N106 side chain maintained stable H-bond contacts with the backbone carbonyls of uL14 residues A133 and A136, with an average donor-acceptor distance of 2.9 Å (**Figures 6A, C**). The sidechain amide oxygen atom in N106 also retained its native intramolecular contacts with R61 (**Figure 6C**), bridging uL14 with the internal network of eIF6 H-bonding interactions spanning blades 1-5, as described above. Thus, simulations of the WT complex demonstrated that the key contacts observed in the cryo-EM structure were largely reproduced (**Figure 4B**). In contrast, similar analysis of the eIF6 mutant revealed significant destabilization around S106. The serine sidechain hydroxyl was only able to form weak, intermittent H-bonds with the backbone carbonyl oxygens of uL14 residues A133 and A136 (**Figures 6B, C**) or the guanidinium moiety of eIF6 R61 (**Figure 6C**). Supporting the apparently weakened eIF6-uL14 interface, an influx of water molecules was observed after ~150 ns in one of the mutant simulation replicas, satisfying the H-bonding potential of the eIF6 S106 sidechain and uL14 A133 and A136 backbone nitrogens (**Figures 6B, D**). These water molecules persisted at the interface throughout the remainder of the simulation, leading to displacement of the eIF6 core relative to uL14, followed by partial solvation of their interaction interface (**Figures 6E, F**). We conclude that comparative MD simulations of the WT and mutant complexes support the hypothesis that the SDS-related eIF6 N106S mutation disrupts the eIF6-uL14 interaction interface and ultimately leads to its solvation, due to the lower propensity for the mutant to satisfy the H-bonding network with uL14.

EIF6* mutations rescue larval lethality of Sbds-deficient *Drosophila

We sought to test the general concept that somatic *EIF6* mutations can effectively rescue the deleterious effects of a hypomorphic germline *Sbds* mutation in a whole animal context by harnessing *Drosophila* genetics. Based on their strength as suppressors of the fitness defect of Sdo1-deleted yeast cells[6], we expressed three eIF6 missense mutations (eIF6-C56R, eIF6-Y151H and eIF6-V192F) that map to the uL14 interaction interface of eIF6 (**Figure 7A**) in Sbds-deficient *Drosophila*.

We initially examined the subcellular localization and function of the *Drosophila* Sbds protein. *Drosophila* Sbds localized to the cytoplasm of ovarian follicle cells and in whole larvae (**Figures 7B, C**) but did not colocalize with the mitotic spindle (**Suppl. Figure 5**). In control experiments, Sbds protein expression was selectively lost in the posterior half of the wing disc in cells expressing $Sbds^{RNAi}$ (marked with GFP) (**Figure 7D).** We conclude that *Drosophila* Sbds is a cytoplasmic protein, consistent with the localization of its mammalian and *Dictyostelium* counterparts[7,8].

To examine the consequences of Sbds deficiency in *Drosophila*, we used RNAi to deplete Sbds in the imaginal disc of the developing wing (denoted $Sbds^{RNAi/+}$ in **Figures 7E, F**). Sbds depletion reduced the surface area of the adult wing by 10 % compared with control (**Figure 7F**). A corresponding 27 % increase in cell number (as assessed by hair density) indicated a decrease in cell size. We next generated mutant ($Sbds^{P/P}$) animals homozygous for the insertion of a PiggyBac-element transposon ($PBac\{WH\}CG8549^{f01686}$) within the 5' untranslated region of the *Sbds* (CG8569) gene, 18 nucleotides upstream of the start codon, on the third chromosome at cytological position 65C3 (**Figure 7G**). In addition, we engineered $Sbds^{P/P}$ mutants expressing three independent eIF6 missense mutants eIF6-C56R, eIF6-Y151H and eIF6-V192F (marked with a MYC tag). Immunoblotting of cell extracts revealed a marked reduction in Sbds protein expression with a concurrent increase in the amount of endogenous eIF6 in homozygous $Sbds^{P/P}$ mutants alone compared with WT or $Sbds^{P/P}$ mutants expressing eIF6-C56R-MYC (**Figure 7H**). Phenotypically, compared with WT or $Sbds^{P/P}$ mutants expressing eIF6-C56R-MYC, $Sbds^{P/P}$ animals alone exhibited a severe growth defect, with only 10 % of third instar larvae surviving to the early pupal stage (**Figure 7I**). Remarkably, all three *EIF6* missense mutant transgenes rescued the viability of the homozygous $Sbds^{P/P}$ mutant animals, allowing a significant proportion to hatch as fertile adults (eIF6-C56R, 18.8 %, n = 182; eIF6-Y151H, 71.7 % n = 350; eIF6-V192F, 33.7 %, n = 53) (**Figure 7J)**; while overexpression of WT eIF6 induced larval lethality of $Sbds^{P/P}$ at the early second instar stage. None of the *EIF6* missense mutant transgenes impaired the viability or fertility of WT *Drosophila*. Importantly, transgenic expression of *Drosophila* or human SBDS rescued the larval lethality of the homozygous $Sbds^{P/P}$ mutants (**Figure 7J**),

confirming that the mutant phenotype was indeed a consequence of loss of Sbds function, attesting to the conservation of SBDS protein function. Immunoblotting of sucrose gradient fractions revealed that expression of the eIF6-C56R mutant rescued the retention of eIF6 on the 60S subunit (**Figure 7K**), the functional impairment of ribosome assembly (**Figure 7K**), the cytoplasmic redistribution of eIF6 (**Figures 7L, M**) and the 76 % reduction in global protein synthesis in circulating hemocytes (as assessed by *in vivo* incorporation of O-propargyl-puromycin (OP-Puro)) (**Figure 7N**) observed in $Sbds^{P/P}$ mutants compared with WT animals. We conclude that eIF6 missense mutations that map to the interface between eIF6 and uL14 can fully and effectively rescue the deleterious effects of a germline hypomorphic *Sbds* mutation in *Drosophila*.

DISCUSSION

In this study, we have identified acquired *EIF6* mutations as a common form of somatic genetic rescue in SDS, a leukemia predisposition disorder caused by a germline defect in ribosome assembly that impairs the release of eIF6 from nascent 60S ribosomal subunits[2,6-8]. These somatic *EIF6* mutations rescue the primary molecular pathological defect in SDS *in vivo*, either by reducing the dose of eIF6 or by lowering the affinity of eIF6 for the 60S subunit.

The development of sensitive and reliable genetic tools has recently enabled the detection of mosaic somatic mutations and spontaneous chromosomal alterations in diverse tissues from normal individuals[11]. A growing number of studies have demonstrated that such somatic genetic modifications accumulate with age and participate in age-related disease, clonal expansion, and cancer development. However, in the context of Mendelian disease, *de novo* genetic events can counterbalance the deleterious effect of germline mutations, providing the somatically modified cells with a selective advantage compared with their non-modified counterparts. This phenomenon of SGR has been reported in Mendelian hematopoietic disorders where it promotes the clonal expansion of SGR positive cells detectable in blood[13]. In the present study, ultra-deep targeted sequencing has revealed

that genetic alterations in the *EIF6* gene that impact the stability or expression of eIF6 or its interaction with the 60S subunit represent a recurrent indirect mechanism of SGR in hematopoietic cells from SDS patients. In agreement with the reported accumulation of somatic genetic alterations over time in hematopoietic cells from normal individuals[5,6], we found that the frequency of independent *EIF6* mutations in SDS positively correlates with increasing age. However, the frequency of somatic mutations over time in hematopoietic cells from normal individuals is still a matter of debate[11]. Strikingly, we detected *EIF6* mutant clones in 4 SDS patients below 10 years of age, one of whom was 3.4 years old. In addition, we detected multiple independent *EIF6* mutant clones (up to 8) in several SDS patients. Together these observations support the idea that the acquisition of somatic mutations in hematopoietic cells is more frequent than previously thought, as they have generally only been unveiled in a context where they provide a selective advantage and promote clonal expansion[11].

Sbds deletion from mesenchymal stem cells in the mouse induces mitochondrial dysfunction, oxidative stress and activation of the DNA damage response (DDR) in HSPCs[9]. These data led to the proposal that mesenchymal inflammation promotes genotoxic stress in SDS HSPCs and drives the evolution to leukemia. However, the mutational signature in our analysis predominantly consists of C>T transitions (**Figure 2E**) that characterize mutations that accumulate with age in normal individuals[5, 6], arguing against a strong contribution, if any, of DDR pathways to the promotion of SGR in SDS bone marrow cells. Since somatic mutations accumulate in tissues outwith the hematopoietic system[4, 11], it will be interesting to determine whether cellular clones with somatic *EIF6* mutations arise in other organs in SDS, a multi-system disorder caused by a germline ribosome assembly defect.

The hematological manifestations in SDS are highly heterogeneous in different individuals who carry identical germline *SBDS* mutations and may even fluctuate within a single individual over time[10]. However, we found no correlation between the presence and/or frequency of *EIF6* somatic mutations and the hematological parameters. Longitudinal analysis will be necessary to determine whether clonal expansion promoted by the acquisition of somatic *EIF6* mutations delays or abrogates

453 the emergence of hematological complications such as aplastic anemia, myelodysplastic syndrome
454 (MDS) or acute myeloid leukemia (AML). Clonal hematopoiesis and progression to poor prognosis
455 MDS or AML in SDS is associated with the acquisition of biallelic somatic *TP53* mutations[11,1242].
456 Single cell sequencing will be required to determine whether individual clones can carry both *EIF6*
457 and *TP53* somatic mutations or whether these variants are mutually exclusive. Further studies are also
458 warranted to examine the effects of *EIF6* and/or *TP53* mutant clones on disease outcome in SDS.

459 Recently Koh et al. reported an individual with clinical features of SDS in whom a *de novo*
460 heterozygous missense *EIF6* mutation (R61L) was identified by whole exome sequencing of
461 peripheral blood leukocytes[43]. The authors concluded that this heterozygous *EIF6* mutation caused the
462 disease. Intriguingly, the eIF6-R61L mutation rescued the fitness defect of Sdo1-deficient yeast cells
463 (**Figure 5F**). Furthermore, the hematological abnormalities observed in the patient described by Koh
464 et al. appeared to improve over time. Given our observation that somatic *EIF6* mutations are frequent
465 in blood cells from SDS patients and can promote clonal expansion, we hypothesize that the *EIF6*
466 mutation identified by Koh et al. is an example of SGR counteracting the deleterious effect of an as
467 yet unidentified germline defect in ribosome assembly (we previously reported that pathogenic
468 mutations affecting the EFL1-encoding gene that cause SDS may be missed by whole exome
469 sequencing[23]). We propose that the selective advantage provided by the somatic *EIF6* mutation
470 promoted expansion of the mutant HSPCs to repopulate the hematopoietic system to a VAF close to
471 50 % in peripheral blood DNA. Similar phenomena have been observed in other Mendelian
472 hematopoietic disorders[14-16]. This hypothesis will need to be tested by sequencing of the *EIF6* gene in
473 tissues other than blood.

474 By combining ultra-deep *EIF6* sequencing, cytogenetic, structural, MD simulations and
475 functional analysis, our study provides evidence that distinct genetic *EIF6* alterations can rescue the
476 germline ribosome assembly defect to promote clonal expansion in SDS HSPCs and achieve SGR
477 (**Figure 8**). We confirmed the presence of an interstitial deletion in chromosome 20 that encompasses
478 *EIF6* in hematopoietic cells from some individuals with SDS[26,28]. However, as the interstitial

chromosomal deletion removed additional genes to *EIF6*, we were unable to formally conclude that expansion of del(20q) clones was a specific consequence of *EIF6* haploinsufficiency. The detection in hematopoietic cells from an SDS patient of a reciprocal translocation in which one of the breakpoints disrupted the *EIF6* gene while the other resided within a non-coding region strongly supports the idea that *EIF6* haploinsufficiency does indeed provide a selective advantage and promotes the clonal expansion of SBDS-deficient cells (**Figure 8**). To our knowledge, SGR induced by a reciprocal translocation has not been previously reported[13]. Lastly, our ultra-deep sequencing analysis pinpointed the existence of frequent and distinct point mutations in the coding sequence of *EIF6* that promoted SGR. Interestingly, we detected several mutations that recurrently affected the same conserved residues. We distinguished three categories of *EIF6* point mutations: (1) nonsense and frameshift mutations that led to *EIF6* haploinsufficiency; (2) missense mutations that affected highly conserved amino-acids and strongly reduced eIF6 expression and/or stability; (3) missense mutation that did not impair eIF6 expression but reduced its affinity for the 60S subunit (e.g. N106S, R61L, G14S) (**Figure 8**). Our MD simulations supported by *in vivo* functional analysis demonstrate that the eIF6 N106S mutant provides a particularly potent selective advantage that is explained by the key structural role of residue N106 in mediating polar interactions between eIF6 and the ribosomal protein uL14 on the intersubunit face of the 60S subunit.

In conclusion, our study demonstrates that spontaneous acquired mutations affecting the *EIF6* gene represent a frequent mechanism of indirect SGR of the germline defect in ribosome assembly in SDS. The demonstration that the recurrent missense mutation N106S promotes SGR by reducing the affinity of eIF6 for the 60S subunit provides a compelling *in vivo* rationale for the development of small molecules that mimic the effects of eIF6 suppressor mutations in reducing the affinity of eIF6 for the 60S subunit as disease modifying therapeutics in SDS. Lastly, our results support the notion that SGR might represent a universal phenomenon, more frequent than previously suspected, that influences the clinical evolution of diverse Mendelian disorders that not only affect the hematopoietic system. Additionally, the phenomenon of SGR may also be frequent in non-inherited disorders as

recently exemplified by chronic liver disease[45]. The continued improvement in sequencing technologies will likely permit the exploration of SGR in many other disorders in the near future.

Materials and Methods

Study approval. Informed and written consent was obtained from donors and patients. The study and protocols comply with the 1975 Declaration of Helsinki as well as with the local legislation and ethical guidelines from the Comité de Protection des Personnes de l'Ile de France II and the French advisory committee on data processing in medical research.

Constructs with human *EIF6*. Coding sequence of WT or mutant human eIF6 was inserted in the linearized (BglII/NotI) p3X-FLAG-Myc-CMV-26 vector (Sigma) to express FLAG-tagged eIF6 protein (**Suppl. Table S5**). The *EIF6* mutations were introduced by hemi-RT-PCR with specific primers (**Suppl. Table S6**). The PCR products and linearized p3X-FLAG-Myc-CMV-26 vector were assembled with NEBuilder® HiFi DNA assembly master mix (New England Biolabs). Nucleotide numbering reflects the cDNA sequence with +1 corresponding to the A of the ATG translation initiation codon in the reference sequence.

Western blotting. 2 x 10^6 HEK 293T were transfected with 3 µg of vectors expressing FLAG-eIF6-WT or FLAG-eIF6-mutants by electroporation (Biorad) or lipofectamine 2000 (Invitrogen). 72 hrs post-transfection, cells were scraped, washed in PBS and lysed for 20 min on ice in lysis buffer containing 50 mmol/L Tris (pH 8.0), 2 mmol/L EDTA, 1 % Triton X100, 1 % phosphatase inhibitor cocktails (Sigma) and protease inhibitor (Roche Applied Science, Indianapolis, IN) and centrifuged; supernatant was harvested and protein concentration quantified using the Bradford assay. Whole-cell lysates were analyzed by immunoblotting with appropriate antibodies using the Odyssey® CLx Imaging System (LI-COR Biosciences) for quantification.

Targeted *EIF6* sequencing by NGS (capture by hybridization approach) and genetic analysis. Genomic DNA was extracted from whole blood cells or bone marrow. Illumina compatible barcoded genomic DNA libraries were constructed according to the manufacturer's sample preparation protocol (Ovation Ultralow V2, Nugen Technologies). Briefly, 400 ng to 3 µg of patient genomic DNA was mechanically fragmented to a median size of 200 bp using a Covaris. 100 ng of double strand fragmented DNA was end-repaired and adaptors containing a Unique Dual Index barcode (IDT) were ligated to the repaired ends (one pair of barcodes per patient). Ligated DNA fragments were PCR amplified to obtain precapture barcoded libraries that are pooled at equimolar concentrations. The capture process was performed using the SureSelect reagents (Agilent), 750 ng of the pool of precapture libraries and home-made biotinylated probes (as previously described in Benyelles et al.[47] and Venot et al.[48]. The biotinylated single stranded DNA probes were designed and prepared to cover a 123 kb chromosomal region including the *ElF6* gene on chromosome 20 (chr20:35,256,992-35,380,631, according to the GRCh38.p12 assembly of the human reference genome) or the *EIF6* cDNA was obtained by PCR amplification with primers located in the 3' and 5' UTR (Sequence (5'->3') F: CGG GGC CTG AGG GAC GGA GG; R: ACA ACA GAG CAG GTT TTT GC). During the capture process, barcoded library molecules complementary to the biotinylated beads were retained by streptavidin coated magnetic beads on a magnet and PCR amplified to generate a final pool of postcapture libraries covering the targeted genomic regions. Pools of these final libraries were prepared and sequenced either on an Illumina HiSeq2500 or NovaSeq6000 (Paired-End sequencing 130+130 on HiSeq, 100+100 bases on NovaSeq, production of ~60 million of clusters per sample). After demultiplexing, sequences were aligned to the reference human genome hg19 using the Burrows-Wheeler Aligner (Li and Durbin, 2010). The mean depth of coverage per sample was >=1,000X to enable more accurate Copy Number Variant Analysis. Downstream processing was carried out with the Genome Analysis Toolkit (GATK), SAMtools and Picard, following documented best practices (http://www.broadinstitute.org/gatk/ guide/topic?name=best-practices). Variant calls were made with the GATK Unified Genotyper. Variants at very low allele frequency were called by freebayes with the option -F 0,0005 (--min_alternate_fraction) (https://arxiv.org/abs/1207.3907). The

annotation process is based on the latest release of the Ensembl database. Variants were annotated, analyzed and prioritized using the Polyweb/PolyDiag software interface designed by the Bioinformatics platform of University Paris Descartes/Imagine Institute.

The sequence analysis dn/ds tool from UCSF (https://humangenetics.ucsf.edu/sequencing-tool/) was used to calculate dN/dS.

Cytogenetics and CGH array. Agilent SurePrint G3 Cancer CGH+SNP 4x180K microarray (Agilent Technologies, Santa Clara, CA) was used for genomic copy number analyses according to manufacturers' recommendations. Genomic positions are relative to the human genome Build NCBI37/hg19. Chromosomal preparation from bone marrow was performed using standard protocols and fluorescence *in situ* hybridization (FISH) was performed using Del (20q) Deletion Probe LPH 020 (Cytocell Ltd, Cambridge, UK) according to manufacturers' recommendations.

Determination of the translocation t(16;20)(q24;q11.2) breakpoints with chimeric reads. To accurately assess the breakpoint location of chromosome 20 / chromosome 16 translocation, we extracted all the reads from chromosome 16 that contain a soft clip in the cigar and determined the position of the last aligned position. We then grouped all those putative break points according to their position to look for clustering. Finally we retained the candidate clusters where mates pointed to chromosome 20 only, and the *EIF6* region in particular, for visual inspection with IGV. The command used was: samtools view -q 1 sample.bam chr16 | cut -f3,4,6-8 | grep S | awk '{pos=$2; split($3,a,"[IMDSH]"); split($3,b,"[0-9]*"); nb=length(b); for (i=2; i<=nb; i++) if (b[i] ~ /[MD]/) pos=pos+a[i-1]; printf("%s\t%s\t%s\t%s\t%s\t%s\n",$1, pos-1, pos-1, $3, $4, $5)}' | sort -k2,2n | bedtools merge -d 0 -c 5,6 -o distinct,distinct | grep -E '=,chr20|chr20,=' | grep -v -E '=,chr20,|chr20,=,' | sort -k5,5n. Study of the reads assigned positions of the breakpoint to a position between 85,849,823 and 85,849,825 (HG19) on chromosome 16 and to a region ranging from 33,867,599 to 33,867,604 on chromosome 20. The translocation was supported by 10 reads on chromosome 16 in total. The boundary was supported by 6 reads where 3 were inter-chromosomal alignment. On chromosome 20, due to the read-depth greater than 1,800, the situation was less clear. However, we identified 10 inter-

chromosomal alignment reads and 15 more reads supporting the breakpoint region. Similar analysis in 4 unrelated controls did not retrieve chimeric reads between chromosome 16 and 20.

Sucrose gradient of human cell extracts. For ribosome fractionation cytoplasmic extracts from HEK293 cells were prepared as already described[13]. For each sample 1 mg of extract was layered on a 10–50 % sucrose gradient containing 20 mM Tris pH 7.6; 80 mM NaCl; 5 mM $MgCl_2$; 1 mM DTT. The gradients were run in an SW41 Beckman rotor at 220,672 *g* for 140 min at 4 °C. Following centrifugation gradients were fractionated. Acquisition of the profiles was obtained using the UA6 UV/VIS detector from ISCO.

Statistical analyses. Statistical analyses were performed on Prism (GraphPad Software). Groups were analyzed by Student t-test as indicated and the difference was considered statistically significant for $p<0.05$. Pearson correlation on Prism (GraphPad Software) was used for correlation determination.

***Dictyostelium* cell cultivation and transfection.** Ax2 (DBS0235521) cells were grown in filter sterilised HL5 (Formedium #HLE2) containing 200 µg/mL Dihydrostreptomycin (Sigma #D7253) in tissue culture dishes or in shaken suspension at 180 revolutions per minute at 22 °C. For transfection, cells were harvested from tissue culture plates and washed by centrifugation twice in ice-cold H40 buffer (40 mM HEPES, 1 mM $MgCl_2$ pH 7.0). They were resuspended at 4 x 10^7 cells/mL and 0.1 mL added to a pre-chilled electroporation cuvette (gap width 2 mm, Geneflow #E6-0062). 1-2 µg of supercoiled or restriction enzyme digested plasmid DNA was added and electroporated with two 350 V square wave pulses each of 8 ms duration delivered 1 s apart using a GenePulser Xcell (Bio-Rad)[14]. Ax2 cells expressing eIF6 or vector (pDM1203) alone were selected in 10 cm tissue culture dishes using 10 µg/mL G418 (Gibco Geneticin #10131-035). Clonal eIF6 knockout cell lines were selected in 96 well tissue culture plates (60 or 600 cells/well) in 0.15 mL of HL5 medium/well containing 10 µg/mL blasticidin (InvivoGen #ant-bl-1) and 10 µg/mL G418. After 7-12 days in selection, confluent wells were harvested, the genomic DNA extracted (Quick-DNA™ Miniprep Kit, Zymo research #D3024) and screened by PCR using oligonucleotides DTO16 and DTO18 that bind to regions of the eIF6 genomic locus that are outside that of knockout cassette (**Suppl. Table S7**) [15].

Plasmid construction. To make knockout vector pDT131 genomic DNA both proximal and distal to the *EIF6* gene were amplified by PCR using primer pairs DTO1/DTO9 and DTO2/DTO3 that introduced restriction enzyme sites for cloning (**Suppl. Table S7**) . The PCR products were digested with ApaI or BamHI/SacII and cloned into pLPBLP either side of the 'floxable' bsR cassette[16] and the inserts verified by sequencing. *Dictyostelium* WT or mutant eIF6 expression plasmids were made by PCR amplification of the eIF6 coding sequence (DDB0234038) from Ax2 genomic DNA with the inclusion of BamHI and XbaI restriction sites. The digested PCR product was cloned into the corresponding restriction sites of extrachromosomal vector pDM1203[17]. The eIF6 T56K, I58T and N106S point mutations were introduced using PCR mediated site-directed mutagenesis. Primer pairs Max15/Max16 were used for T56K, DTO28/DTO29 for I58T and DTO30/DTO31 for N106S. All mutations were verified by sequencing.

Cell Lysis for ribosome profiles. Vegetative cells were treated with 100 µg/mL cycloheximide for 5 min prior to harvesting. Cells were pelleted by centrifugation and resuspended in buffer KK_2 (16.5 mM KH_2PO_4, 3.9 mM K_2HPO_4, 2 mM $MgSO_4$) plus 100 µg/mL cycloheximide. They were washed twice more in KK2 , with a final wash in KK_2 containing 100 µg/mL cycloheximide and 1x SigmaFast EDTA-free protease inhibitor cocktail (Sigma #S8830). The cell pellet was resuspended at 2 $x10^8$/mL in 50 mM HEPES pH 7.5, 40 mM $Mg(CH_3COO)_2$, 25 mM KCl, 5 % sucrose, 0.4 % IGEPAL® CA-630 (Sigma #I8896), 100 µg/mL cycloheximide, 1x SigmaFast EDTA-free protease inhibitor cocktail, 2 mM PMSF and lysed by passing through a 25 mm diameter Swin-Lok filter holder (GE Healthcare Life Sciences #420200) containing a prefilter (Millipore #AP1002500) together with a 5 µm nucleopore track-etched membrane (Whatman #110613). The lysate was cleared by centrifugation (8,000 *g* for 30 min at 4 °C) and the supernatant passed through a 33 mm Millex-® GV 0.22 µm PVDF filter unit (Millipore #SLGV033RS). The filtrate was divided into 1.4 mL aliquots after A_{260} determination, flash frozen in liquid N_2 and stored at -80 °C. All buffers were at 4 °C.

Sucrose density gradients. Lysates were loaded onto a 10-40 % (w/v) sucrose gradient in 50 mM Hepes pH 7.5, 25 mM $K(CH_3COO)_2$, 40mM $Mg(CH_3COO)_2$ in Polyallomer 14 x 95 mm centrifuge

633 tubes (Beckman). After centrifugation (Beckman SW40Ti rotor) at 260, 900 *g* for 3 hr at 4 °C,
634 gradients were fractionated at 4 °C using a Gilson Minipuls 3 peristaltic pump with continuous
635 monitoring (A_{254} nm) and polysome profiles recorded using a Gilson N2 data recorder. Proteins were
636 precipitated from 0.5 mL fractions using 20 % (v/v) trichloroacetic acid, separated on SDS–PAGE
637 gels and transferred to nitrocellulose membranes for immunoblotting.

638 **Subcellular fractionation.** Vegetative cells in mid-log phase were harvested, washed in KK2 buffer
639 and resuspended at 2 x 10^7 cells/mL. One mL of cells was pelleted by centrifugation and lysed in NLB
640 buffer (50 mM Tris-HCl pH 7.4, 5 mM Mg $(CH_3COO)_2$, 10 % (w/v) sucrose, 2 % (v/v) NP-40 by
641 vortexing for 1 min. Nuclei were pelleted by centrifugation at 2300 *g* for 5 min at 4 °C and the
642 supernatant saved as the "crude cytoplasmic" fraction. The nuclear pellet, washed once in 1 mL of
643 NLB and resuspended in 100 µL of NLB, was designated the "nuclear fraction."

644 **Immunoblotting.** *Dictyostelium* cells were resuspended at 2 x 10^7 cells/ mL in 1 x NuPAGE® sample
645 buffer (Invitrogen #NP0007) containing 5 % (v/v) 2-mercaptoethanol (Sigma #M6250) and heated at
646 95 °C for 3 min. 2 x 10^5 cell equivalents were loaded per well of a NuPAGE™ 4-12 % Bis-Tris gel
647 and resolved in 1 x MES SDS running buffer (Life technologies #NP0002). SeeBlue® Plus2
648 (Invitrogen #LC5925) or HiMark™ (ThermoFisher scientific #LC5699) prestained standards were
649 used to calibrate each gel. The iBlot 2 Dry Blotting System (Invitrogen™ #IB21001) was used to
650 transfer the proteins to nitrocellulose membranes (Invitrogen #IB23001). The membranes were
651 blocked for 30 min in block buffer (PBS containing 0.1 % (v/v) TWEEN®20 (Sigma #T2700) and 5
652 % (w/v) dried skimmed milk powder). The primary antibody was diluted in block buffer and
653 incubated with the blocked membrane for 2-4 hr at room temperature or overnight at 4 °C. The
654 membrane was washed for 10 min with gentle agitation in PBS-T buffer (PBS containing 0.1 % (v/v)
655 TWEEN®20) and this was repeated another 3 times with fresh PBS-T. The secondary antibody was
656 diluted in block buffer and incubated with the washed membrane for 1-2 hr at room temperature. The
657 blot was developed in 1.5 mL of Immobilon® Western chemiluminescent HRP substrate (Millipore

658 #WBKLS0500) according to the manufacturer's instructions. The membranes were visualized with the
659 ChemiDoc™ MP imaging system (BIO RAD) using Image Lab software (BIO RAD).

660 **Yeast Strains, plasmids and primers**. *S. cerevisiae* strains used in this study are listed in **Suppl**.
661 **Table S8**, primers are listed in **Suppl. Table S9**, and plasmids in **Suppl. Table S10**. To create the
662 *Sdo1*$^{int(ts)}$ strain, the conditional TS18 intein[7,18]was amplified by PCR from plasmid pS5DH-G4MINT
663 (gift from N. Perrimon) and inserted between the *SDO1* codons for K73 and C74 by homologous
664 recombination. For the generation of Tif6-GFP mutants, site-directed mutagenesis of the pTIF6-GFP
665 plasmid was performed using the Phusion High-Fidelity PCR kit (NEB) and transformed into XL1-
666 Blue Electroporation-Competent cells (Agilent).

667 **Growth assays.** *sdo1*^{ts} yeast cells were grown in SD –URA liquid medium at 23 °C to stationary
668 phase. 2 OD_{600} of cells were harvested and re-suspended in 500 µL mQ water. 2 µL of serial tenfold
669 dilutions were spotted onto solid SD–URA medium and growth was assessed after 2 d of culture at 30
670 °C, or 3 d at 23 °C or 37 °C.

671 **Immunoblotting.** The *sdo1*^{ts} yeast cells were grown at 23 °C to an OD_{600} of 0.8-1 in SD–URA liquid
672 medium. 1 OD_{600} of cells were harvested, washed and re-suspended in 500 µL of mQ water. 50 µL of
673 1.85 M NaOH was added and the samples incubated on ice for 10 min. Samples were further
674 incubated on ice with 17.5 µL of 100 % (w/v) of TCA and centrifuged for 5 min at 16,000 *g*. The
675 pellet was washed with 500 µL of 80 % acetone (v/v) and centrifuged for 5 min at 16,000 *g*. The
676 supernatant was decanted and the resultant pellet air-dried. The pellet was resuspended in 1x NuPAGE
677 LDS sample buffer (Thermo Fisher Scientific) containing 50 mM DTT prior to incubation at 70 °C for
678 10 min. Samples were separated using the NuPAGE 4-12 % Bis-Tris gel (Thermo Fisher Scientific)
679 containing 1x MES buffer (Thermo Fisher Scientific). Proteins were transferred from the gel to the
680 nitrocellulose membrane using the iBlot 2 (Thermo Fisher Scientific) system. The nitrocellulose
681 membrane was blocked with 5 % (w/v) milk dissolved in PBST buffer (137 mM NaCl, 2.7 mM KCl,
682 4.3 mM Na_2HPO_4, 1.47 mM KH_2PO_4 with 0.1 % (v/v) Tween 20) for 30 min. The blot was incubated
683 with 1:1000 dilution of anti-eIF6 antibody (GenTex, #GTX117971) overnight at 4 °C followed by

several 5 min washes with PBST buffer. The blot was incubated with 1:5000 dilution of anti-rabbit IgG HRP-linked antibody (Cell Signaling #7074) followed by several 5 min washes with PBST buffer. 1 mL of Luminol and 1 mL of Peroxide solution from the Western Chemiluminescent HRP Substrate kit (Immobilon) was incubated with the blot for 1 min. Proteins were visualized using the Bio-Rad Chemidoc MP imaging system.

Genetic complementation. These were performed as previously described[6].

***Drosophila melanogaster* strains and genetics.** Flies were maintained using standard culture techniques. All crosses were performed at 25 °C unless otherwise stated. Fly strains and genotypes are described in **Suppl. Table S4**. *CG8549*^{f01686}, *PBac{WH}CG8549[f01686]*, referred to here as *Sbds*^{P}, is a homozygous lethal piggyBac transposase element insertion in the 5′ untranslated region of *CG8549*.

Transgenic *Drosophila* lines. The coding sequences for WT *Drosophila Sbds* (NM_139800) and *EIF6* (NM_145105) were amplified by PCR from a *Drosophila* embryo cDNA library (gift from Simon Bullock) and cloned into pTWF (The Drosophila Gateway vector collection) to generate plasmids pUAS-Sbds-FLAG and pUAS-EIF6-FLAG. *EIF6* suppressor mutations, *EIF6C56R, EIF6Y151H* and *EIF6V192F* were generated by PCR site-directed mutagenesis and sub-cloned into vector pPWM (The *Drosophila* Gateway vector collection) using the Gateway system (Invitrogen). Transgenic *pUAS-Sbds-FLAG, pUAS-EIF6-FLAG, pUAS-EIF6C56R-MYC, p-UAS-EIF6Y151H-MYC* and *pUAS-EIF6V192F-MYC* flies were generated by P element–mediated germline transformation[19] into a w^{1118} strain by Genetic Services Inc. To generate flies expressing human SBDS, the coding sequence for human SBDS (NP_057122) was PCR amplified from a pRSETA-SBDS plasmid[8] and sub-cloned into plasmid pTWF to generate plasmid pUAS-SBDS-FLAG. Transgenic *pUAS-SBDS-FLAG* flies were generated as described above. Primers are listed in **Suppl. Table S11**.

Antibodies. Antibodies are listed in **Suppl. Table S12**. Rabbit polyclonal antiserum was raised against *Drosophila* Sbds residues 1-252 and affinity purified (Eurogentec).

Protein expression and purification. Plasmid pSbds-His (encoding *Drosophila* Sbds, amino acids 1-252, fused at the C-terminus to 6 x His residues) was transformed into *E. coli* C41(DE3) cells and Sbds-6xHis protein was purified by Ni-NTA affinity (GE Healthcare) and a Hiload 26/60 Superdex 75 column (GE Healthcare). Protein purity was assessed by SDS-PAGE and identity confirmed by mass spectrometry.

Immunofluorescence. Wing discs dissected from third-instar larvae and ovaries dissected from adult female flies were fixed in 4 % paraformaldehyde in PBS for 30 min at room temperature and processed for immunofluorescence (IF) staining as described[20,21]. For IF staining of mitotic cells in neuroblasts, *Drosophila* brain squash slides were prepared as described[22]. Primary antibodies are listed in **Suppl. Table S12**. Alexa 488 (green)- or 563 (red)- or 647 (far red)- conjugated secondary antibodies (Invitrogen) were used at 1:1000 dilution. DNA was stained with DAPI in mounting medium (Vector). Images were collected on a Zeiss LSM780 confocal system, imported to Image J v10.4 (Image J) and Photoshop CS5 (Adobe), and adjusted for brightness and contrast uniformly across entire fields.

Immunoblotting. *Drosophila* larval extracts were prepared by grinding ten third instar larvae in 150 µL NuPAGE LDS sample buffer (Invitrogen, #NP0007) using a pellet pestle (Eppendorf). Samples were cleared in a microfuge and denatured by heating at 95 °C for 10 min. Third instar larvae cells were fractionated using NE-PER nuclear and cytoplasmic extraction reagents (Thermo Scientific, #78833) according to the manufacturer's instructions. Cell lysates were cleared in a microfuge and normalized for protein concentration using a BCA protein assay kit (Pierce, #23227). Samples were separated using SDS-PAGE for immuno-blotting.

Sucrose gradient sedimentation of *Drosophila* cell extracts. Ribosomal subunits were separated by sucrose density gradients as previously described[8]. Briefly, *Drosophila* third instar larvae were collected (typically 40 mg), washed with PBS, homogenized in lysis buffer A (10 mM Tris-HCl at pH 7.4, 10 mM NaCl, 2.5 mM $MgCl_2$, 0.5 % (v/v) Triton X-100, 0.5 % (w/v) deoxycholate, 1 % (v/v) Tween 20, 100 mg/mL cycloheximide (Sigma, #C7698) with complete EDTA-free protease inhibitors

(Roche) and 0.5 U/mL RNase inhibitor (Promega) and incubated for 10 min on ice. Lysates were cleared in a microcentrifuge. Equal amounts (typically 3-5 A_{254} U) were applied to a 10-50 % (w/v) sucrose gradient in 14 mL of buffer B (10 mM Tris-HCl at pH 7.4, 75 mM KCl, 2.5 mM $MgCl_2$) and centrifuged (Beckman SW40 rotor) at 284, 600 *g* for 2 hr at 4 °C). Samples were loaded on a Brandel gradient fractionator, the polysome profiles were detected using a UV monitor (UV-1, Pharmacia) at A_{254}, and 0.5 mL fractions collected. The electronic outputs of the UV-1 monitor and fraction collector were fed into a Labjack U3-LV data acquisition device with an LJTick-InAmp preamplifier. Proteins were precipitated from sucrose gradient fractions with 10 % (v/v) trichloroacetic acid (TCA), separated on SDS-PAGE gels and transferred to PVDF membranes for immuno-blotting.

Measurement of protein synthesis. Protein synthesis in *Drosophila* cells was measured using an adapted protocol[2,23]. Briefly, about thirty third instar larvae were dissected in culture medium (Shields and Sang M3 insect medium (Sigma, #S3652), 10 % fetal bovine serum (Sigma, #F7524) and 1 % Penicillin-Streptomycin (Pen-Strep, Sigma, #P0781)) within 10 min and hemocytes collected into a 1.5 mL tube. An equal volume of culture medium with 100 µM of OP-Puro (Invitrogen, #C10456) was added to the hemocytes and incubated at 25 °C for 30 min. Cells were collected by centrifugation at 2, 500 *g* for 4 min, and washed twice with ice-cold phosphate buffered saline (PBS) (Invitrogen) with 1 % BSA (Sigma) and 100 µg/mL cycloheximide (Sigma, #C7698). Cells were fixed and permeabilized using the Cytofix/Cytoperm Fixation Permeabilization Kit (BD Biosciences, #554714). Azide-alkyne cycloaddition was performed using the Click-iT Cell Reaction Buffer Kit (Invitrogen, #C10456) with azide conjugated to Alexa Fluor 488 at 5 µM final concentration. Following a 30 min reaction, cells were washed twice in PBS, resuspended in PBS supplemented with 1 % fetal bovine serum and analysed by flow cytometry (Becton Dickinson LSR Fortessa analyzer). Flow cytometry data analysis was performed using FlowJo v10.1 (FlowJo, Ashland, OR). 'Relative protein synthesis rate' was calculated by normalizing OP-Puro signals to control cells after subtracting background fluorescence (cells without OP-Puro incorporation).

Molecular dynamics simulations

System setup. The atomic model for MD simulations was based on the cryo-EM structure of the human 60S-eIF6 complex at 2.4 Å resolution (PDBID: XXXX). The protein-RNA complex comprised: i) eIF6 residues M1-N225; ii) eL24 residues M1-K60; iii) uL3 residues A45-P82, P206-T223 and H275-R378; iv) uL14 residues S10-A140; and v) 28S rRNA bases A4589-G4639, G4660-U4677 and A4473-U4482. System setup was carried out using the CHARMM-GUI web server [24-26]. Proteins and RNA were inserted into a cubic box (dimension 11.2 nm), allowing a minimum of 1 nm distance from the box edges. Solvation using TIP3P water and sufficient potassium and chloride ions to neutralize the system, to a final, physiologically representative salt concentration of 0.1 M.

Simulation protocol. All simulations were performed using GROMACS v2019.6[27] with the CHARMM36 additive force field[28]. Energy minimization was performed using the steepest descent algorithm (<5,000 steps) to remove steric clashes, and a 4 ns equilibration phase followed with all protein and RNA atoms were position-restrained with gradually reducing force constants to relax the system, ranging from 400 to 40 kJ $mol^{-1}nm^{-2}$. All dihedral angles were restrained during equilibration using a force constant of 4 kJ mol^{-1} nm^{-2}. Production simulations were carried out in the NPT ensemble for 500 ns in triplicate for all systems. During production runs, position restraints were applied to uL3 (backbone atoms of residues P82, P206, T223 and H275) and the 28S RNA (main chain atoms of bases A4589, G4639, G4660, U4677 and A4473-U4482) to maintain the tertiary structure of uL3 and prevent unfolding of the 28S rRNA. A 2 fs integration time step was used and trajectory frames were written every 20 ps. All covalent bonds hydrogens were constrained using the LINCS algorithm[29]. Long-range electrostatics were treated with the Particle-Mesh-Ewald algorithm using a real space cutoff of 1.2 nm[30]. Lennard-Jones interactions were smoothly switched off between 1.0 and 1.2 nm. The Nosé-Hoover thermostat was utilized to maintain the temperature at 303.15 K with a coupling constant of 1 ps[31,32]. Protein and RNA were coupled separately from the solvent. Isotropic pressure coupling was applied at 1 bar using the Parrinello-Rahman barostat with a coupling constant of 5 ps and compressibility of $4.5x10^{-5}$ bar^{-1} [33,34].

Simulation Analysis. The VMD software was used for trajectory visualization and figure preparation[35]. All analysis was performed using integrated tools within the GROMACS package[27]. The Grace plotting tool and the GNU Image Manipulation Program (GIMP) were utilized to visualize the plots.

Acknowledgements. We thank the patients and their families. P.R. thanks Dr Loélia Babin (Genome dynamics in the Immune system lab, Imagine Institute) for her assistance with graphical representation of mutational landscape and Lolliplot. P.R. thanks Serge Romana and Marc Le Lorch (Hôpital Necker-Enfants malades, Paris France) for the kind gift of the BAC (BAC CTD-2094A15) containing the complete *EIF6* gene.

Author contribution. L.K., A.B., J.M., and P.R. generated constructs and performed functional experiments in human models. B.B.,C.B-C., J.D., J-A.M., and F.D. identified the affected patients and performed related clinical studies. S.K. and I.R-W. performed cytogenetic analysis. S.F. conducted sucrose gradients on human cells. C.B-F., O.A., A.P., M.P., M.Z., performed deep sequencing. P.N., C.M. and F.T. conducted bioinformatics analysis. I.C. performed structural analysis. A.J.W. conceived and B.G, N.E-U, A.Z.B., A.F., C.H., M.R., D.T. and S.T. performed experiments in yeast, *Dictyostelium* and *Drosophila*. V.K. performed molecular dynamics simulations with input from P.J.B. P.R. conceived the genetic project and did the sequencing analysis. P.R. and A.J.W. wrote the manuscript with editing contributions from J-P.V., I.C., D.T., C.H., V.K. and S.T.

Funding. This work has been supported by institutional grants from INSERM, Ligue Nationale contre le Cancer (Equipe Labellisée La Ligue 'LIGUE 2020'), and CEREDIH (Centre de Référence Déficits Immunitaires Héréditaires). This work was supported by State funding from the Agence Nationale de la Recherche under "Investissements d'avenir" program (ANR-10-IAHU-01). This study contributes to the IdEx Université de Paris ANR-18-IDEX-0001. P.R. is a scientist from Centre National de la Recherche Scientifique (CNRS). A.J.W. was supported by a Specialist Programme from Blood Cancer UK (12048, to AJW), the UK Medical Research Council (MR/T012412/1), a Wellcome Trust strategic award to the Cambridge Institute for Medical Research (100140), a core support grant from the

Wellcome Trust and MRC to the Wellcome Trust-Medical Research Council Cambridge Stem Cell Institute, the Connor Wright Project, the Cambridge National Institute for Health Research Biomedical Research Centre and the European Cooperation in Science and Technology (COST) Action CA18233 "European Network for Innovative Diagnosis and treatment of Chronic Neutropenias, EuNet INNOCHRON".

Conflict of interest: The authors declare that there are no competing financial interests in relation to the work described.

References

1. Blokzijl, F. *et al.* Tissue-specific mutation accumulation in human adult stem cells during life. *Nature* **538**, 260-264 (2016).

2. Martincorena, I. & Campbell, P.J. Somatic mutation in cancer and normal cells. *Science* **349**, 1483-1489 (2015).

3. Garcia-Nieto, P.E., Morrison, A.J. & Fraser, H.B. The somatic mutation landscape of the human body. *Genome biology* **20**, 298 (2019).

4. Martincorena, I. Somatic mutation and clonal expansions in human tissues. *Genome medicine* **11**, 35 (2019).

5. Osorio, F.G. *et al.* Somatic Mutations Reveal Lineage Relationships and Age-Related Mutagenesis in Human Hematopoiesis. *Cell Rep* **25**, 2308-2316 e2304 (2018).

6. Lee-Six, H. *et al.* Population dynamics of normal human blood inferred from somatic mutations. *Nature* **561**, 473-478 (2018).

7. Terao, C. *et al.* Chromosomal alterations among age-related haematopoietic clones in Japan. *Nature* **584**, 130-135 (2020).

8. Machiela, M.J. *et al.* Mosaic chromosome 20q deletions are more frequent in the aging population. *Blood advances* **1**, 380-385 (2017).

9. Loh, P.R. *et al.* Insights into clonal haematopoiesis from 8,342 mosaic chromosomal alterations. *Nature* **559**, 350-355 (2018).

10. Jaiswal, S. & Ebert, B.L. Clonal hematopoiesis in human aging and disease. *Science* **366** (2019).

11. Vijg, J. & Dong, X. Pathogenic Mechanisms of Somatic Mutation and Genome Mosaicism in Aging. *Cell* **182**, 12-23 (2020).

12. Weill, J.C. & Reynaud, C.A. Somatic Darwinism in vivo. *Bio Systems* **12**, 23-25 (1980).

13. Revy, P., Kannengiesser, C. & Fischer, A. Somatic genetic rescue in Mendelian haematopoietic diseases. *Nat Rev Genet* **20**, 583-598 (2019).

14. McDermott, D.H. *et al.* Chromothriptic cure of WHIM syndrome. *Cell* **160**, 686-699 (2015).

15. Le Guen, T. *et al.* An in vivo genetic reversion highlights the crucial role of Myb-Like, SWIRM, and MPN domains 1 (MYSM1) in human hematopoiesis and lymphocyte differentiation. *J Allergy Clin Immunol* **136**, 1619-1626 (2015).

16. Catto, L.F.B. *et al.* Somatic genetic rescue in hematopoietic cells in GATA2 deficiency. *Blood* **136**, 1002-1005 (2020).

17. Maryoung, L. *et al.* Somatic mutations in telomerase promoter counterbalance germline loss-of-function mutations. *J Clin Invest* **127**, 982-986 (2017).

18. Gutierrez-Rodrigues, F. *et al.* Pathogenic TERT promoter variants in telomere diseases. *Genet Med* **21**, 1594-1602 (2018).

19. Benyelles, M. *et al.* NHP2 deficiency impairs rRNA biogenesis and causes pulmonary fibrosis and Hoyeraal-Hreidarsson syndrome. *Hum Mol Genet* **29**, 907-922 (2020).

20. Warren, A.J. Molecular basis of the human ribosomopathy Shwachman-Diamond syndrome. *Adv Biol Regul* **S2212-4926**, 30153-30157 (2017).

21. Boocock, G.R. *et al.* Mutations in SBDS are associated with Shwachman-Diamond syndrome. *Nat Genet* **33**, 97-101 (2003).

22. Stepensky, P. *et al.* Mutations in EFL1, an SBDS partner, are associated with infantile pancytopenia, exocrine pancreatic insufficiency and skeletal anomalies in a Shwachman-Diamond like syndrome. *J Med Genet* **54**, 558-566 (2017).

23. Tan, S. *et al.* EFL1 mutations impair eIF6 release to cause Shwachman-Diamond syndrome. *Blood* **134**, 270-290(2019).

24. Finch, A.J. *et al.* Uncoupling of GTP hydrolysis from eIF6 release on the ribosome causes Shwachman-Diamond syndrome. *Genes Dev* **25**, 917-929 (2011).

25. Menne, T.F. *et al.* The Shwachman-Bodian-Diamond syndrome protein mediates translational activation of ribosomes in yeast. *Nat Genet* **39**, 486-495 (2007).

26. Pressato, B. *et al.* Deletion of chromosome 20 in bone marrow of patients with Shwachman-Diamond syndrome, loss of the EIF6 gene and benign prognosis. *British journal of haematology* **157**, 503-505 (2012).

27. Valli, R. *et al.* Different loss of material in recurrent chromosome 20 interstitial deletions in Shwachman-Diamond syndrome and in myeloid neoplasms. *Mol Cytogenet* **6**, 56 (2013).

28. Valli, R. *et al.* Shwachman-Diamond syndrome with clonal interstitial deletion of the long arm of chromosome 20 in bone marrow: haematological features, prognosis and genomic instability. *British journal of haematology* **184**, 974-981 (2019).

29. Dror, Y. Shwachman-Diamond syndrome. *Pediatric blood & cancer* **45**, 892-901 (2005).

30. Bellanne-Chantelot, C. *et al.* Mutations in SRP54 gene cause severe congenital neutropenia as well as Shwachman-Diamond-like syndrome. *Blood* **132**, 1318-1331 (2018).

31. Kircher, M. *et al.* A general framework for estimating the relative pathogenicity of human genetic variants. *Nat Genet* **46**, 310-315 (2014).

32. Martincorena, I. *et al.* Tumor evolution. High burden and pervasive positive selection of somatic mutations in normal human skin. *Science* **348**, 880-886 (2015).

33. Welch, J.S. *et al.* The origin and evolution of mutations in acute myeloid leukemia. *Cell* **150**, 264-278 (2012).

34. Martincorena, I. *et al.* Universal Patterns of Selection in Cancer and Somatic Tissues. *Cell* **171**, 1029-1041 e1021 (2017).

35. Bassler, J. *et al.* Interaction network of the ribosome assembly machinery from a eukaryotic thermophile. *Protein science : a publication of the Protein Society* **26**, 327-342 (2017).

36. Gartmann, M. *et al.* Mechanism of eIF6-mediated inhibition of ribosomal subunit joining. *The Journal of biological chemistry* **285**, 14848-14851 (2010).

37. Groft, C.M., Beckmann, R., Sali, A. & Burley, S.K. Crystal structures of ribosome anti-association factor IF6. *Nature structural biology* **7**, 1156-1164 (2000).

38. Morini, J. *et al.* Radiosensitivity in lymphoblastoid cell lines derived from Shwachman-Diamond syndrome patients. *Radiation protection dosimetry* **166**, 95-100 (2015).

39. Zambetti, N.A. *et al.* Mesenchymal Inflammation Drives Genotoxic Stress in Hematopoietic Stem Cells and Predicts Disease Evolution in Human Pre-leukemia. *Cell stem cell* **19**, 613-627 (2016).

40. Donadieu, J., Beaupain, B., Fenneteau, O. & Bellanne-Chantelot, C. Congenital neutropenia in the era of genomics: classification, diagnosis, and natural history. *British journal of haematology* **179**, 557-574 (2017).

41. Brina, D., Miluzio, A., Ricciardi, S. & Biffo, S. eIF6 anti-association activity is required for ribosome biogenesis, translational control and tumor progression. *Biochimica et biophysica acta* **1849**, 830-835 (2015).

42. Xia, J. *et al.* Somatic mutations and clonal hematopoiesis in congenital neutropenia. *Blood* **131**, 408-416 (2018).

43. Koh, A.L. *et al.* Heterozygous missense variant in EIF6 gene: A novel form of Shwachman-Diamond syndrome? *American journal of medical genetics. Part A* (2020).

44. Miluzio, A. *et al.* Impairment of cytoplasmic eIF6 activity restricts lymphomagenesis and tumor progression without affecting normal growth. *Cancer cell* **19**, 765-775 (2011).

45. Zhu, M. *et al.* Somatic Mutations Increase Hepatic Clonal Fitness and Regeneration in Chronic Liver Disease. *Cell* **177**, 608-621 e612 (2019).

46. Ziemiecki, A., Muller, R.G., Fu, X.C., Hynes, N.E. & Kozma, S. Oncogenic activation of the human trk proto-oncogene by recombination with the ribosomal large subunit protein L7a. *The EMBO journal* **9**, 191-196 (1990).

47. Benyelles, M. *et al.* Impaired telomere integrity and rRNA biogenesis in PARN-deficient patients and knock-out models. *EMBO molecular medicine* **11**, e10201 (2019).

48. Venot, Q. *et al.* Targeted therapy in patients with PIK3CA-related overgrowth syndrome. *Nature* **558**, 540-546 (2018).

FIGURE 1

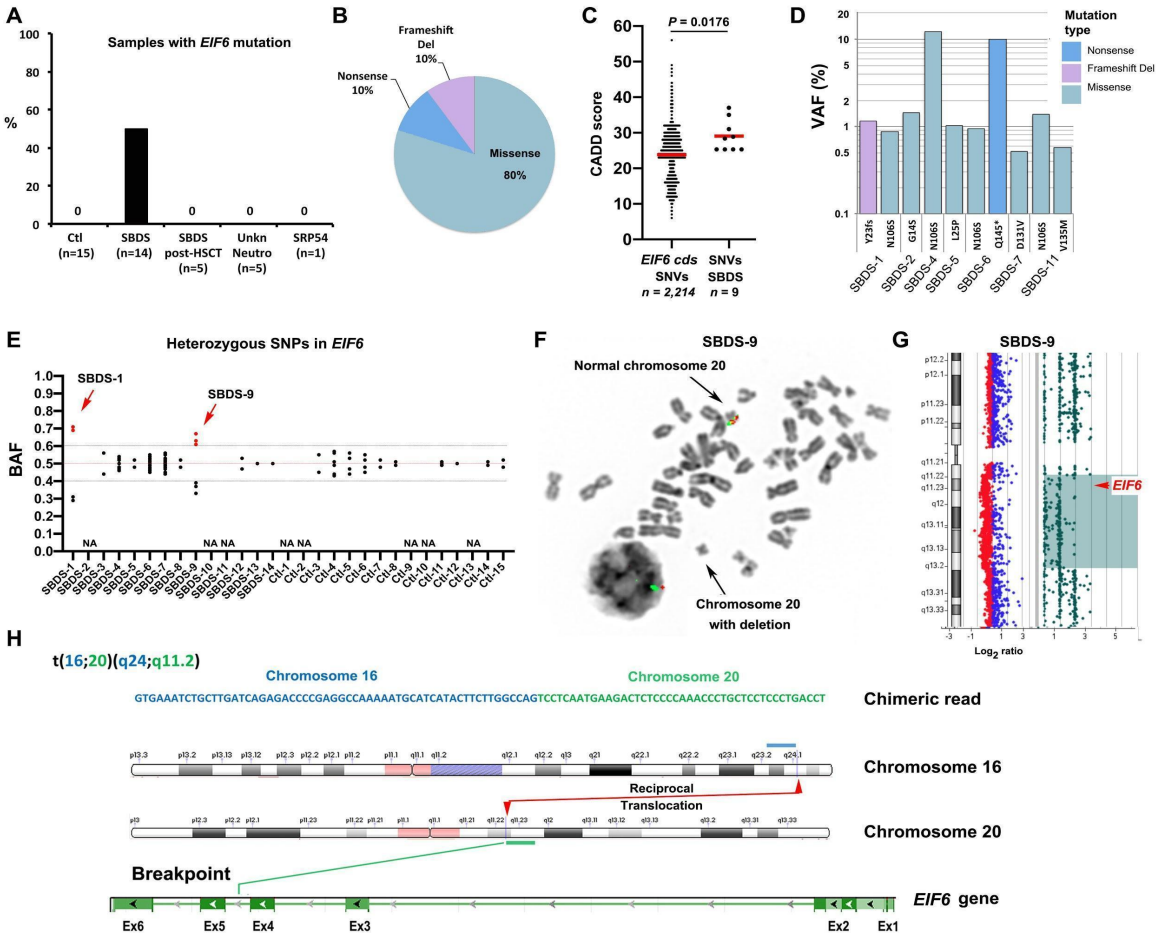

Figure 1. Multiple somatic genetic events target the *EIF6* gene in hematopoietic cells in SDS.

(**A**) Somatic *EIF6* mutations are common in SDS. Percentage of individuals with EIF6 mutations in the specific groups of patients is indicated. (**B**) Classification of identified *EIF6* mutations. (**C**) CADD scores of all the possible SNVs in the coding sequence of *EIF6* (n = 2,214; **Suppl. Table S2**) versus the 9 SNVs in *EIF6* identified in SDS patients. P-value of unpaired t test is indicated. (**D**) VAF of the 10 identified *EIF6* mutations identified in the indicated SDS patients. (**E**) BAF of the heterozygous single nucleotide polymorphisms (SNPs) located in *EIF6* in SDS patients and healthy controls. NA: not available. (**F**) Detection of interstitial del(20q) by metaphase cytogenetics with fluorescent probes located 7 Mb downstream of the *EIF6* gene in bone marrow cells from patient SBDS-9 (**Suppl. Fig. 1**). (**G**) Large heterozygous mosaic genomic deletion on chromosome 20 encompassing the *EIF6* gene (red arrow) detected by array comparative genomic hybridization (CGH) in bone marrow cells from patient SBDS-9. (**H**) Identification of the breakpoint in the reciprocal translocation t(16; 20)(q24; q12) within intron 4-5 of *EIF6* on chromosome 20q. Chromosome 16 sequence is blue, chromosome 20 is green.

FIGURE 2

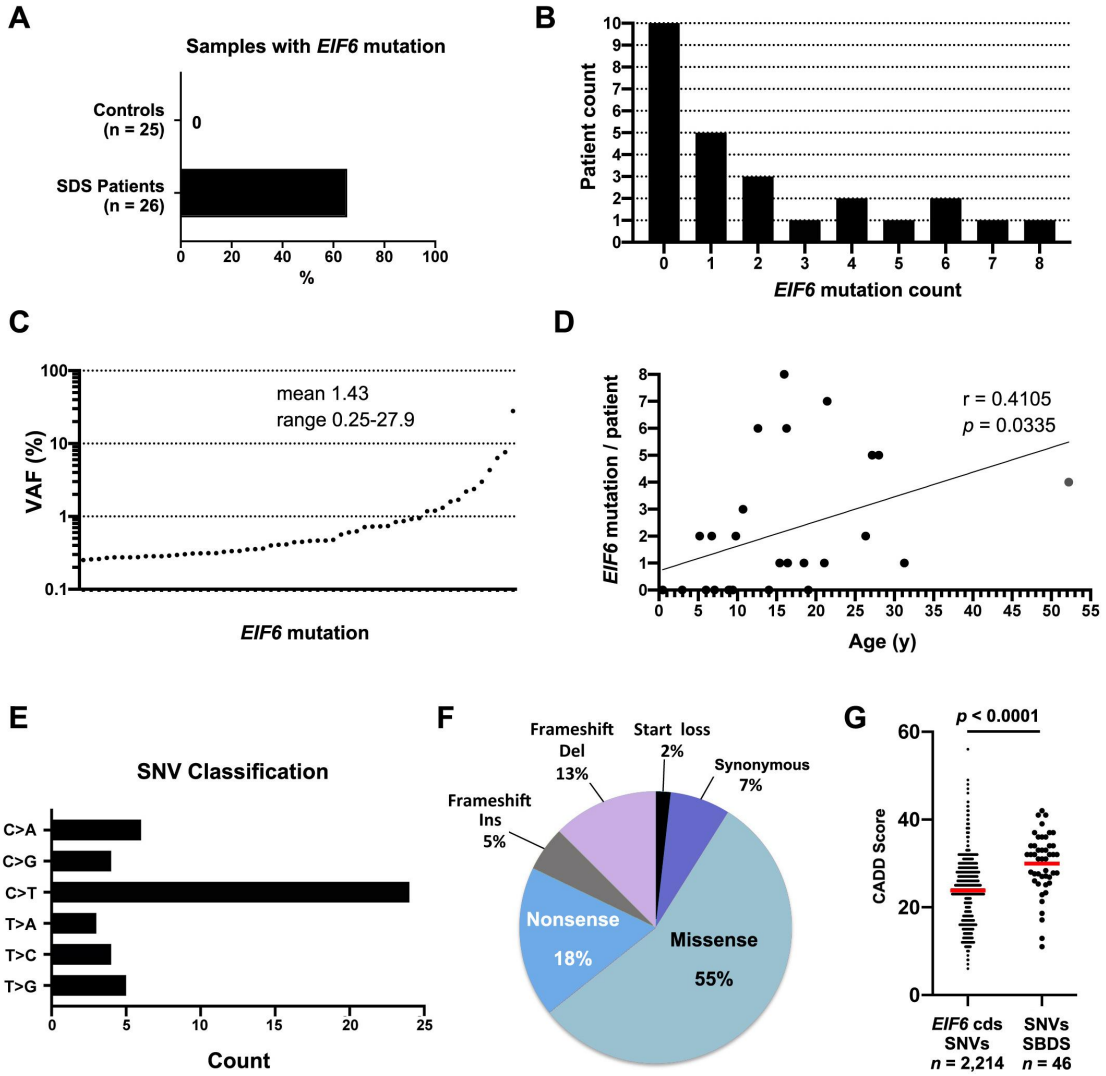

Figure 2. **Somatic *EIF6* mutations identified in SDS.** (**A**) Percentage of SDS patients carrying somatic *EIF6* mutations. (**B**) *EIF6* mutation count across the 26 SDS patients. (**C**) VAF distribution of the 56 identified *EIF6* mutations detected by ultra-deep sequencing. (**D**) Mutation count in each individual versus age. (**E**) Mutational spectrum of the 46 SNVs identified in *EIF6*. P-value and Pearson correlation are indicated. (**F**) Classification of the 56 mutations identified in *EIF6*. (**G**) CADD scores of all the possible SNVs (n = 2,214; **Suppl. Table S2**) in *EIF6* coding sequences versus the CADD scores of the 46 SNVs identified in the SDS patients. P-value of unpaired t test is indicated.

968 **FIGURE 3**

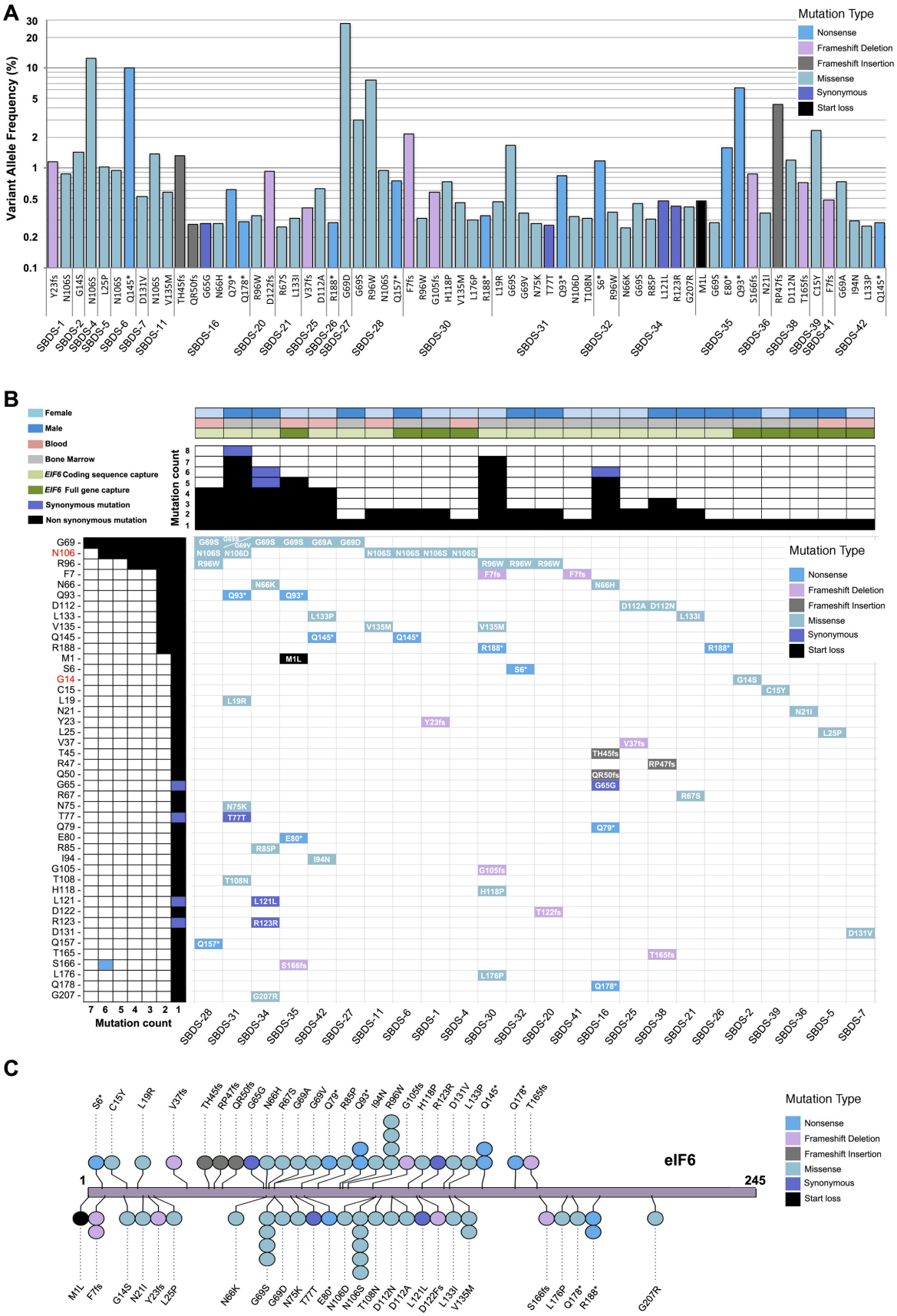

969

Figure 3. Spectrum of somatic *EIF6* mutations in SDS hematopoietic cells. (**A**) Spectrum of 66 mutations and their corresponding VAFs identified by ultra-deep sequencing in 24 SDS patients. (**B**) Waterfall plot of the 66 mutations highlighting the recurrently impacted residues. N106S and G14S (highlighted in red on the left) represent gain-of-function mutations identified in Sdo1-deleted yeast cells[25]. Gender of patients, origin of DNA, and method of *EIF6* capture for deep-sequencing are indicated. Purple cases represent synonymous mutations. Colors denote type of mutation as listed in the inset (upper right corner). (**C**) Lolliplot showing the distribution of mutations in eIF6.

FIGURE 4

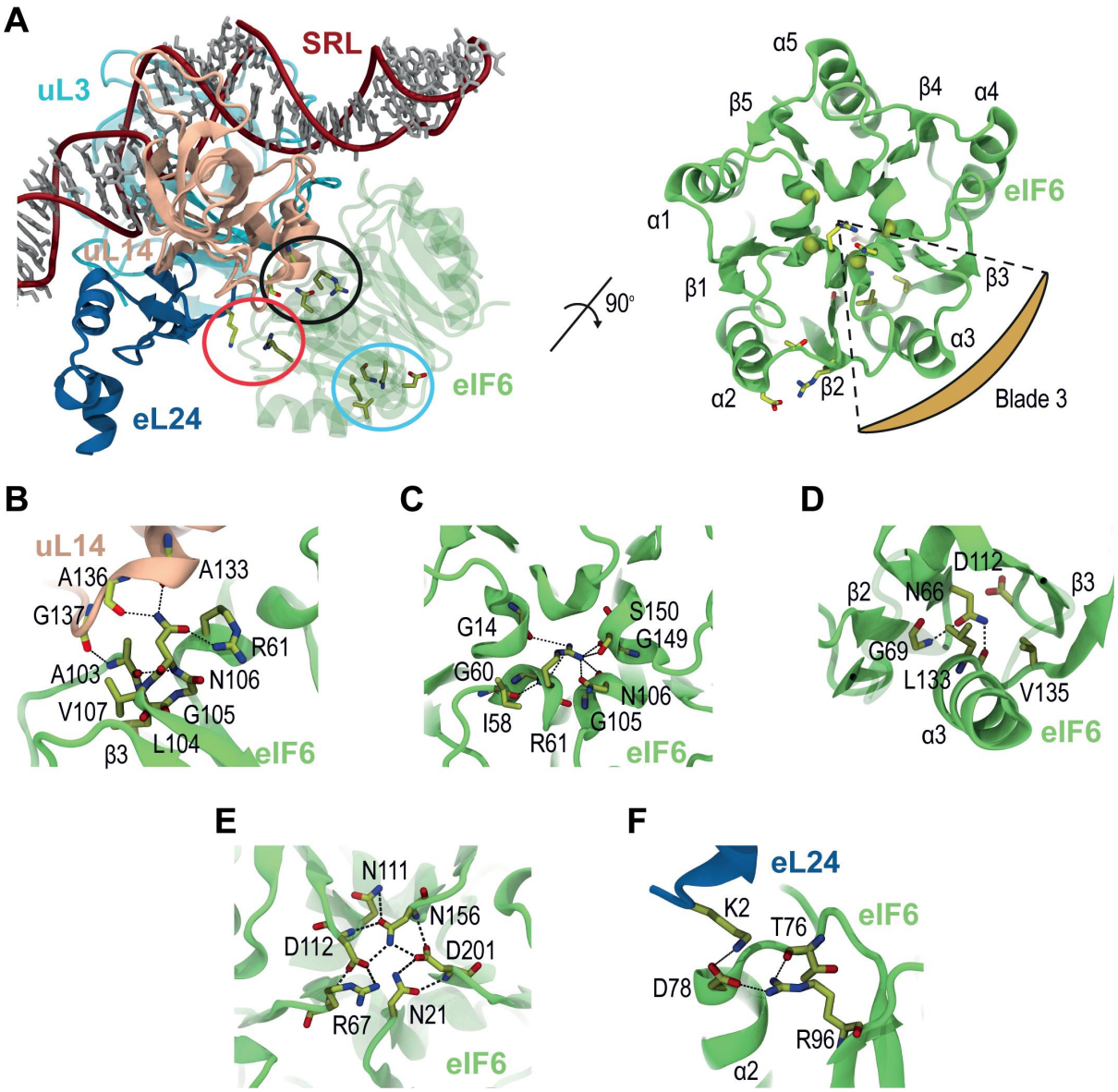

Figure 4. SDS-related eIF6 mutations map to three hotspots. (**A**) Atomic model (two orthogonal views) of the interface between human eIF6 and the 60S ribosomal subunit. The eIF6 residues mutated in SDS cluster in three independent hotspots highlighted in black (interface with uL14), cyan (interface between blades 2 and 3) and red (eL24 interface) ellipses. (**B-F**) Stabilizing interactions formed by SDS-related eIF6 residues N106 (**B**), R61 (**C**), N66, G69, L133, V135 (**D**), D112 (**E**), and R96 (**F**). eL24 is blue; uL14, salmon; eIF6, green. SRL, sarcin-ricin loop.

FIGURE 5

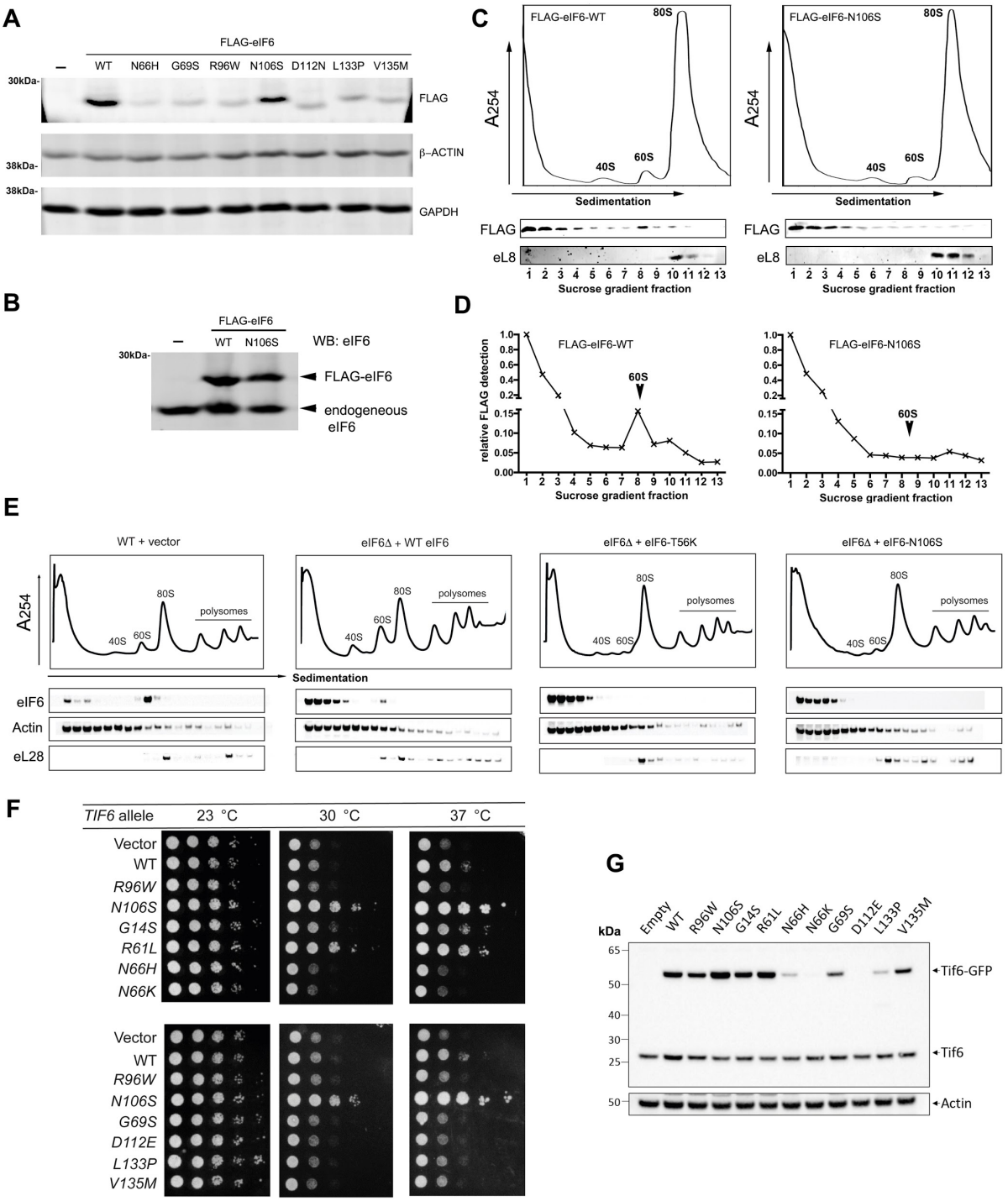

Figure 5. Functional consequences of SDS-related eIF6 mutations. (**A, B**) The eIF6-N106S mutation does not alter eIF6 protein stability in human cells. Cell extracts from HEK293T cells were immunoblotted to detect the indicated FLAG-eIF6 variants compared with (**A**) GAPDH, β-ACTIN or (**B**) endogenous eIF6. Representative of three independent experiments. (**C**) The N106S mutation

reduces eIF6 affinity for the 60S subunit in human cells. Cell extracts from HEK293T cells transfected with FLAG-eIF6-WT or FLAG-eIF6-N106 were fractionated by sucrose gradient sedimentation and immunoblotted to visualize eIF6 or eL8. Representative of two independent experiments. (**D**) Quantification of FLAG-eIF6 expression in the experiments depicted in (**C**). (**E**) The eIF6-N106S mutant has lower affinity for the 60S subunit in *Dictyostelium* cells. Extracts from eIF6-deleted (*EIF6Δ*) *D. discoideum* Ax2 cells transformed with plasmids expressing eIF6-N106S or eIF6-T56K variants versus WT cells transformed with vector alone were fractionated by sucrose gradient sedimentation and immunoblotted to visualize the indicated proteins. (**F**) SDS-related Tif6 missense variants rescue the fitness defect of Sdo1-deficient cells. Tenfold serial dilutions (from left to right) of conditional Sdo1-deficient (*sdo1^{ts}*) cells complemented with plasmids expressing empty vector (pRS316), WT Tif6 or the indicated Tif6 variants were spotted onto SD-URA medium at the permissive (23 °C, 3 days) or restrictive (30 °C, 2 days; 37 °C, 3 days) temperatures. (**G**) SDS-related Tif6 missense mutations that map to the uL14-binding interface do not alter protein stability. Cell extracts from *sdo1^{ts}* cells expressing empty vector, WT or mutant Tif6-GFP were immunoblotted to detect Tif6 or actin loading control.

FIGURE 6

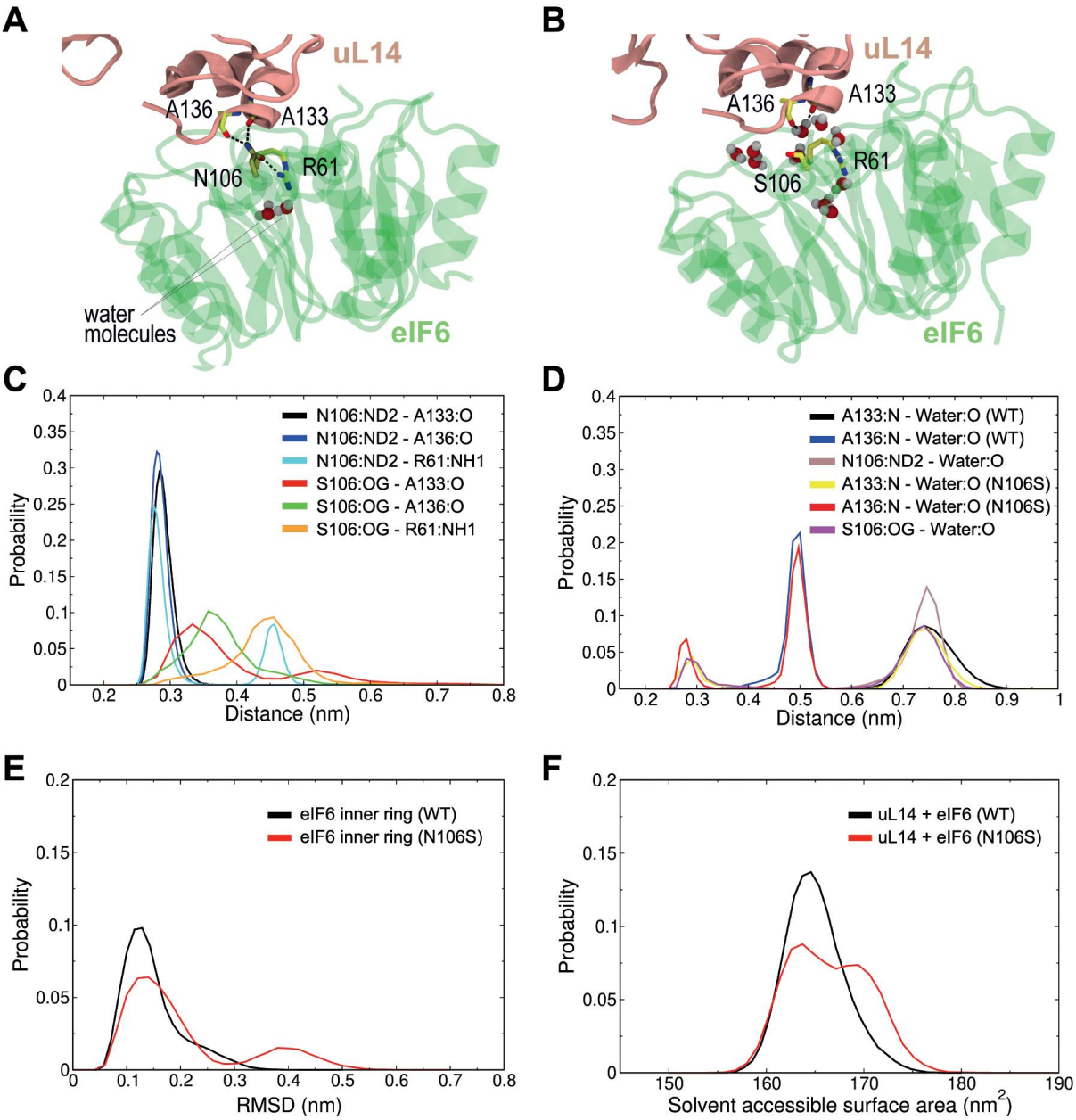

Figure 6. N106S mutation disrupts the H-bonding capacity of the eIF6-uL14 interaction interface. (**A, B**) Representative snapshots of the interaction interface between eIF6 N106 WT or S106 mutant (green) and uL14 (salmon) after 500 ns of simulation. Key water molecules are indicated in CPK format. (**C, D**) Distances (nm) between the indicated atoms of eIF6 WT and mutant (residues N106, S106 and R61), and either uL14 (residues A133, A136) (**C**) or water (**D**). (**E**) Root mean square deviation (RMSD) of the distance (nm) between the WT or mutant eIF6 inner ring and uL14. (**F**) Solvent accessible surface area of the WT or mutant eIF6-uL14 complex. Curves in each plot include data from all 3 replicas per system.

FIGURE 7

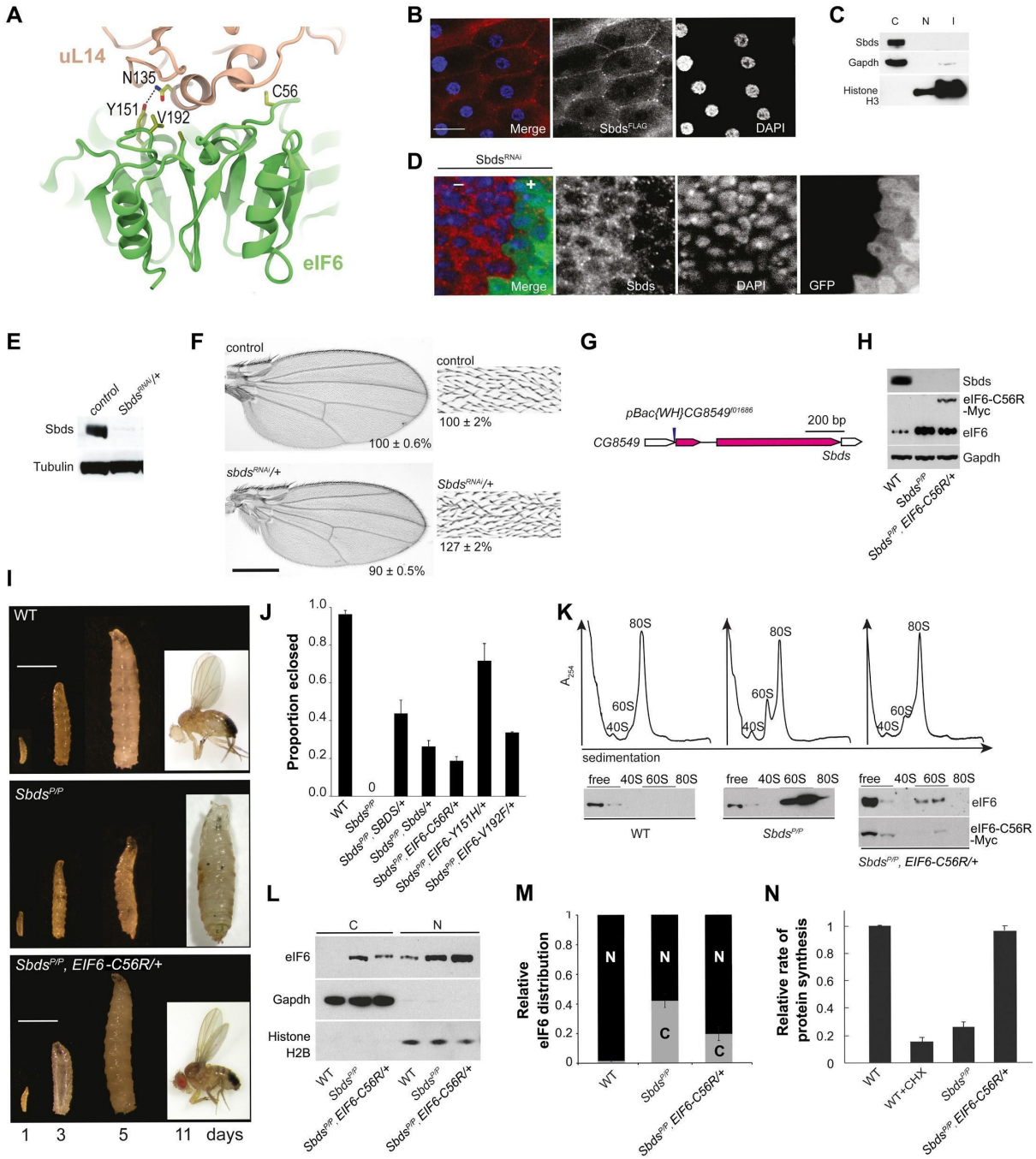

Figure 7. eIF6 missense mutations fully rescue the larval lethality of Sbds-deficient *D. melanogaster*. (**A**) eIF6 residues C56, V192 and Y151 lie at the interface with uL16. eIF6 is colored green; uL14, salmon. (PDBID: XXX) (**B-D**) Cytoplasmic localization of *Drosophila* Sbds revealed by (**B**) immunostaining of FLAG-tagged Sbds (red) in ovarian follicle cells, nucleus shown in blue (DAPI); (**C**) immunoblotting of subcellular fractions from *Drosophila* third instar larvae cells labeled (C)

cytoplasmic, (N) soluble nuclear and (I) insoluble nuclear fraction containing nucleoli and chromatin; (**D**) indirect immunofluorescence of third instar larval wing disc cells. Sbds (red) was depleted by RNAi in posterior wing disc cells (marked with GFP); nucleus is blue, (DAPI). (**E**) RNAi depletion of Sbds in third instar larval extracts revealed by immunoblotting. (**F**) *Sbds* is required for cellular growth. RNAi depletion of *Sbds* in developing wings versus control. Wing size ($n = 15$, $p < 0.0001$, left) and bristle density ($n = 10$, $p < 0.0001$, right) expressed as a percentage (± SE) of control. Scale bar, 200 μm. (**G**) Genomic organisation of the *Drosophila Sbds* (*CG8549*) locus with PiggyBac-element insertion site indicated in blue. White boxes, untranslated regions of *Sbds* mRNA; magenta, *Sbds* coding region; grey line, intron. (**H**) Sbds depletion in homozygous $Sbds^{P/P}$ and $Sbds^{P/P}$*, EIF6-C56R/+* mutants revealed by immunoblotting. (**I**) Three independent eIF6 missense mutations rescue the larval lethality of *Sbds*-deficient flies. Indicated genotypes shown at indicated time-points after fertilization. Scale bar, 1 mm. (**J**) Genetic complementation of Sbds-deficient flies. Proportion of eclosed flies with the indicated genotypes is quantified. (**K**) *EIF6-C56R* rescues the ribosome assembly defect in *Sbds*-deficient flies. Polysome profiles from the indicated fly genotypes are shown. The indicated proteins are visualised by immunoblotting. (**L**) *EIF6-C56R* rescues the cytoplasmic redistribution of eIF6 in Sbds-deficient flies. Subcellular fractions of third instar larvae cells with the indicated genotypes were immunoblotted to visualize the indicated proteins. (**M**) Subcellular distribution of endogenous eIF6 in the indicated genotypes quantified by densitometry of (**L**). Error bars, mean ± SE, n=6, from three replicates. (**N**) *EIF6-C56R* rescues the protein synthesis defect in Sbds-deficient flies. Relative rates of *ex-vivo* OP-Puro incorporation in the indicated genotypes are shown. *Drosophila* genotypes are listed in **Suppl. Table S4**.

FIGURE 8

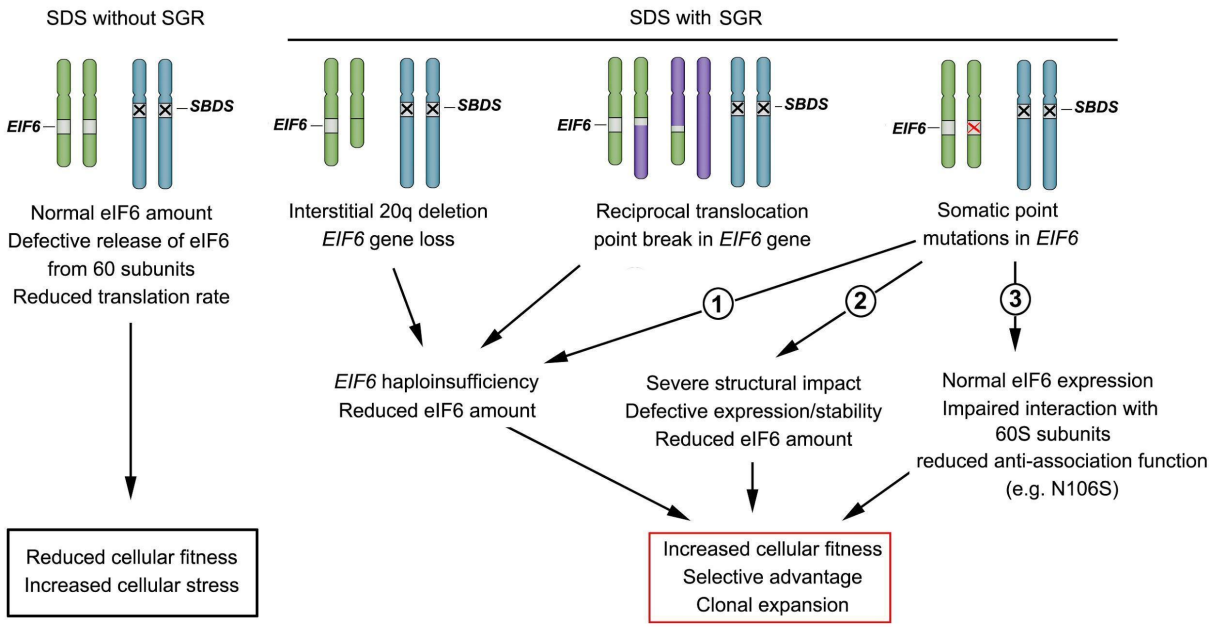

Figure 8. Schematic representation of *EIF6* somatic genetic rescue mechanisms in SDS.